7 Radiative forcing and climate impacts caused by the 2022 Hunga volcano eruption

Lead authors	Georgiy Stenchikov Mark R. Schoeberl
Co-authors	Ewa M. Bednarz Eric Fleming Yi Huang Ilaria Quaglia Pasquale Sellitto Claudia Timmreck Matthew Toohey Jun Wang Zhihong Zhuo
Contributing authors	Peter Colarco David Plummer Takashi Sekiya Simone Tilmes Xinyue Wang Shingo Watanabe Wandi Yu Jun Zhang

Cite this as:

Stenchikov, G., M. R. Schoeberl et al. (2025): Radiative forcing and climate impacts caused by the 2022 Hunga volcano eruption. In APARC, 2025: The Hunga Eruption Atmospheric Impacts Report [Yunqian Zhu, Graham Mann, Paul A. Newman, William Randel (Eds.)]. APARC Report No. 11, WCRP Report No. 10/2025, DOI: [DOI-goes-here], available at `[project-website-or-landing-page]`.

Key points

Radiative Forcing

- **Hunga's stratospheric sulfate aerosol (SA) loading following the eruption was small compared to significant climate-impacting eruptions like the 1991 Mt. Pinatubo eruption**. The initial reported observed amount of SO_2 released in the major emission pulse on 15 January 2022 was 0.5 Tg. Global climate models require 0.65-1.0 Tg of SO_2 to produce stratospheric aerosol optical depths (SAOD) comparable with observations. This higher SO_2 value is consistent with later eruption estimates. Hunga's sulfate aerosol layer stayed in the stratosphere for less than two years.
- **Hunga injected significant amounts of water vapour (WV) into the mid-stratosphere, which will remain in the stratosphere for 4-7 years and could very slightly contribute to warming of the Earth's climate.** A portion of Hunga's water vapour layer was lifted by the Brewer-Dobson Circulation (BDC) into the upper stratosphere and, therefore, persisted in the stratosphere longer than volcanic aerosols. The Hunga water vapour layer decreases the outgoing longwave (LW) radiation at the top of the atmosphere (TOA) and increases the LW downward flux at the tropopause.
- **The net Hunga radiative forcing (RF) was dominated by SA in the first two years. The net global average volcanic RF was about -0.4 ± 0.1 W/m^2, averaged for the two years following the eruption.** At all atmospheric levels, the negative RF caused by SA is an order of magnitude larger than Hunga's WV positive RF during the first two years after the eruption.
- **The WV-induced middle and upper stratospheric cooling (-0.2 K Day^{-1}) is stronger and more persistent than the stratospheric heating by Hunga's SA**. The WV cooling in the 10-30 hPa layer weakened in the two years after the eruption as the Hunga's water vapour ascends, disperses, and is partially removed from the stratosphere.
- **Stratospheric temperature and ozone changes in the Southern Hemisphere only slightly modified the RF**. The reduction in ozone increases the downward short wave (SW) flux at the tropopause, warming the troposphere. Stratospheric temperature adjustment (cooling) reduces the outgoing LW radiation at TOA, warming the climate system. However, during the first two years following the Hunga eruption, the contributions of ozone and stratospheric temperature adjustments to the TOA radiative forcing are significantly smaller than that of SA.
- **Beyond 2024, the Hunga aerosol loading has largely disappeared, and the stratospheric water vapour TOA RF is negligible (<0.005 W m^{-2}).**

Climate Perturbations

- **It is estimated that the Hunga eruption cooled the global average surface air temperature (SAT) by 0.05 K, but this reduction is so subtle as to be indistinguishable from the natural variability of the current climate.**
- **Beyond 2024, once the SA loading has dissipated, the residual warming from Hunga-injected water vapour will be minimal and unable to counteract the accumulated cooling from SAs.** The overall perturbation to global average climate is indistinguishable from natural climate variability.
- **Hunga-induced ozone perturbations and stratospheric cooling from WV may drive regional changes in tropospheric circulation**. Stratospheric meridional temperature gradient changes can impact the troposphere through stratosphere-troposphere dynamic coupling. Ozone depletion-driven cooling of the polar stratosphere in both hemispheres has the potential to strengthen winter polar vortices and delay stratospheric final warming. While these effects are evident in model simulations, their amplitudes remain below the threshold necessary for clear attribution in observations.

Contents

- 7.1 Mechanisms of volcanic climate impacts . . . 160
  - 7.1.1 Impacts of volcanic sulfate aerosols . . . 160
  - 7.1.2 Impact of volcanic water vapour . . . 161
  - 7.1.3 Stratospheric chemistry and dynamics feedbacks . . . 161
  - 7.1.4 The 2022 Hunga eruption . . . 161
- 7.2 Hunga's radiative forcing agents . . . 162
  - 7.2.1 Hunga's sulfate aerosol perturbation . . . 162
  - 7.2.2 Hunga's water vapour perturbation . . . 163
  - 7.2.3 Hunga's ozone perturbation . . . 164
- 7.3 Hunga's radiative forcing . . . 164
  - 7.3.1 IRF, ERF, and SARF . . . 164
  - 7.3.2 Clear sky and all sky RF . . . 165
  - 7.3.3 Hunga's sulfate aerosol and water vapour IRF . . . 166
  - 7.3.4 Empirically calculated ERF . . . 167
  - 7.3.5 Model calculated ERF . . . 167
  - 7.3.6 Uncertainty in radiative forcing . . . 170
- 7.4 Hunga's climate impact . . . 171
  - 7.4.1 SA-dominated climate response (2022-2023) . . . 171
  - 7.4.2 WV-dominated climate response (2024-2030) . . . 173
  - 7.4.3 Indirect atmospheric effects . . . 174
  - 7.4.4 Uncertainties in climate response . . . 176
- 7.5 Discussion and conclusions . . . 176

Preamble

Chapter 7 assesses the tropospheric and climate impacts of the Hunga eruption. The chapter focuses on the radiative forcing associated with the Hunga volcanic eruption and its effect on tropospheric temperatures, as well as indirect effects related to ozone and temperature changes in the stratosphere. Because many of the observed stratospheric changes following the Hunga eruption are detailed in previous chapters, this chapter is closely linked to Chapters 3–5. Chapter 7 also uses the results of HTHH-MOC (see Supplementary S1 and S3) analysis to quantify Hunga's radiative forcing and climate impact, as well as the results of published empirical and modelling studies.

7.1 Mechanisms of volcanic climate impacts

Explosive volcanic eruptions release sulfur-bearing gases, volcanic ash, water vapour (WV), halogens, and other trace substances into the atmosphere, disrupting stratospheric chemistry. The injection altitude can vary from the lower stratosphere (LS, below 25 km) to the upper stratosphere (US, above 25 km), though most stratosphere-reaching eruptions inject material primarily into the LS. Sulfur gases such as SO_2 and H_2S undergo oxidation to form sulfate aerosols (SAs), which can persist in the stratosphere for several years, significantly impacting Earth's radiative balance.

Volcanoes emit large amounts of solid particles, i.e. volcanic ash. Ash comprises recondensed silicate particles with diameters typically larger than 2 μm. While ash usually settles out of the stratosphere within one to two weeks after an eruption, it can generate a short-lived but measurable radiative forcing (RF) (Niemeier et al., 2009; Stenchikov et al., 2021). However, no significant ash particles were observed in the Hunga eruption plume (see Chapters 1 and 2; Legras et al., 2022; Sellitto et al., 2022; Kloss et al., 2022; Baron et al., 2023).

If the eruption is sufficiently large in terms of SO_2 emission (>5 Tg), it can have noticeable effects on atmospheric temperatures, ocean heat content, and both atmospheric and oceanic circulation (Hansen, 2002; Robock, 2000; Timmreck, 2012; Stenchikov, 2016; Swingedouw et al., 2017; Marshall et al., 2022). The estimated Hunga SO_2 emission was between 0.5–0.7 Tg (Carn et al., 2022) based on satellite observations of SO_2 and the amount of sulfate aerosol that formed after the eruption.

7.1.1 Impacts of volcanic sulfate aerosols

Sulfate aerosol particles are typically not emitted directly by volcanic eruptions but instead form in the stratosphere through oxidation of SO_2 followed by the binary nucleation of sulfuric acid and water vapour. This process is followed by particle coagulation, condensational growth, and gravitational settling (Turco et al., 1982; Pueschel, 1996; Hamill et al., 1997). The typical timescale for the conversion of SO_2 to sulfate (SO_4) is about one month (Bluth et al., 1992; Read et al., 1993; Höpfner et al., 2015; Wang et al., 2013). However, the conversion rate can vary depending on the stage of the process and is influenced by factors such as water vapour availability and injection altitude (Höpfner et al., 2015; LeGrande et al., 2016; Carn et al., 2016; Zhu et al., 2022; Abdelkader et al., 2023).

SAs can significantly disrupt the planet's radiative energy balance, impacting stratospheric and tropospheric temperatures and the circulation (Lambert et al., 1993; Baran and Foot, 1994; Bluth et al., 1997; Barnes and Hofmann, 1997; Lacis et al., 1992; Perlwitz and Graf, 2001; Kremser et al., 2016). SAs scatter shortwave (SW) radiation in the entire solar spectrum, increasing the planetary albedo. SAs absorb solar near-IR (NIR) and longwave (LW, λ>4 μm) radiation.

SAs are dispersed throughout the stratosphere by eddies and the Brewer-Dobson Circulation (BDC) (Holton et al., 1995). In the tropical stratosphere, their movement is also influenced by the Quasi-Biennial Oscillation (QBO) (Trepte and Hitchman, 1992). The tropical upward branches of BDC and buoyancy generated by aerosol radiative heating can loft aerosols against gravitational settling, increasing their residence time. The residence time of tiny (< 0.1 μm) background aerosol particles in the stratosphere is about two to three years (Hamill et al., 1997). The residence time of stratospheric volcanic SAs is shorter than background aerosols due to their larger particle size (Deshler, 2008), which increases gravitational sedimentation rates. For example, an analysis of SA observations suggests a mean stratospheric aerosol lifetime from the 1991 Pinatubo eruption of around 22 months and tropical eruptions have longer lifetimes than extra-tropical eruptions (Toohey et al., 2025). Models simulate the formation of SAs using a variety of parametrisation schemes. This leads to discrepancies between models on the SA size distributions and the subsequent SA's radiative properties and residence time (Quaglia et al., 2023; Kremser et al., 2016; Timmreck et al., 2018).

Direct instrumental observations of the radiative forcing of SAs are rare (Dutton and DeLuisi, 1983; Dutton and Christy, 1992; Dutton et al., 1994; Minnis et al., 1993; Russell et al., 1993; Andersson et al., 2015; Solomon et al., 2011). Overall, stratospheric SAs have a net cooling effect on Earth's surface and the troposphere by reducing solar radiation while warming the stratosphere by absorbing NIR and infrared (IR) radiation. Solar spectral irradiance is relatively weak at wavelengths longer than 2.5 µm, where SAs are absorptive, resulting in relatively modest NIR heating by SAs. Consequently, IR radiative heating rates within the aerosol layer are roughly twice as large as those from SW heating. However, the volcanic SW RF at the top of the atmosphere (TOA) dominates over the LW RF (Stenchikov et al., 1998). The stratospheric heating caused by volcanic aerosols' LW and NIR absorption cannot be neglected because it influences stratospheric temperature and circulation patterns (Graf et al., 1994; Kodera, 1994; Thompson and Wallace, 1998; Stenchikov et al., 2002).

7.1.2 Impact of volcanic water vapour

Water vapour is the most abundant gas emitted through volcanic eruptions. The amount of water vapour in the volcanic plume can be significantly enhanced by entraining environmental water (Guo et al., 2004a; Guo et al., 2004b; Joshi and Jones, 2009). The amount of WV that remains in the stratosphere is influenced by the ambient temperature at the injection plume height. Lower stratospheric temperatures range from 180 to 230 K, but temperature increases with altitude, reaching around 270 K near the stratopause (~50 km). At lower temperatures, ice particles form and sediment downwards if the water vapour concentration exceeds the temperature-dependent nucleation threshold. Because stratospheric temperatures rise rapidly with altitude, higher injection levels within the stratosphere lead to greater retention of water vapour, resulting in higher stratospheric water vapour concentrations. For example, the 1991 Pinatubo eruption injected over 80 Tg of water vapour just above the tropopause; however, this vapour quickly condensed and was almost entirely removed through the sedimentation of ice crystals (Stenchikov et al., 2021; Abdelkader et al., 2023; Guo et al., 2004a; Guo et al., 2004b).

Enhanced concentrations of WV in a volcanic plume can also accelerate the conversion of SO_2 to sulfate (LeGrande et al., 2016; Abdelkader et al., 2023). Strong volcanic eruptions could potentially heat the tropopause via SA NIR and IR absorption, increasing tropospheric water vapour entering the stratosphere. While simulations have demonstrated this effect (Joshi and Shine, 2003; Robock et al., 2009; Kroll et al., 2021; Kroll and Schmidt, 2024), it has not yet been observed in real-world situations, including the 1991 Mt. Pinatubo eruption (Fueglistaler et al., 2013; Randel et al., 2004; Chiou et al., 2006).

7.1.3 Stratospheric chemistry and dynamics feedbacks

Ozone is a radiatively active tracer, absorbing solar ultraviolet (UV) and visible radiation and emitting and absorbing IR radiation primarily in a band centred at 9.6 µm. Chemically driven changes in ozone thus can lead to changes in stratospheric heating rates and temperatures. Changes in the meridional temperature gradient in the stratosphere, driven by the radiative effects of SA, WV, or ozone, can alter stratospheric circulation and trigger dynamical interactions between the stratosphere and troposphere (Graf et al., 1994; Kodera, 1994; Thompson and Wallace, 1998; Stenchikov et al., 2002; Maycock et al., 2013). The induced dynamical changes can alter the distribution of other chemical species. Volcanic radiative processes may also change the phase, strength, and duration of El Niño-Southern Oscillation (ENSO) (Predybaylo et al., 2017; Pausata et al., 2015), as well as the strength of the Atlantic Meridional Overturning Circulation (AMOC) (Stenchikov et al., 2009).

7.1.4 The 2022 Hunga eruption

The shallow-underwater eruption of Hunga was unusual in that it increased the WV content in the stratosphere by 10–15% (see Chapters 2 and 3). The Hunga eruption was rated as a Volcanic Explosivity Index (VEI) 6 eruption (see Chapter 1; Newhall and Self 1982; Carn et al. 2022). Hunga's SO_2 emission in the primary eruption on 15 January 2022 was relatively small compared to climatologically significant eruptions such as the VEI 6 1991 Pinatubo eruption. Initial estimates place Hunga's SO_2 release in the major pulse at around 0.5 Tg (Carn et al., 2022; Duchamp et al., 2023). If we account for smaller SO_2 injections before the primary eruption, the total SO_2 reaches 0.7 Tg (Carn et al., 2022), but the smaller emissions dispersed to a lower altitude than the main eruption. From the perspective of SO_2 emissions alone, Hunga's climate impact would likely resemble eruptions with moderate SO_2 output, e.g., St. Helens (1980, 0.875 Tg SO_2), Calbuco (2015, 0.4 Tg SO_2), Raikoke (2019, 1.4

Tg SO_2), Sarychev (2009, 1.2 Tg SO_2), all of which have had a negligible climate impact.

7.2 Hunga's radiative forcing agents

7.2.1 Hunga's sulfate aerosol perturbation

As already noted, the Hunga eruption injected a modest amount of SO_2 in the upper stratosphere and lower mesosphere (Carn et al., 2022; Taha et al., 2022; Witze, 2022; Sellitto et al., 2024), increasing by a factor of ~5–10 the background stratospheric sulfur burden. By comparison, the 1991 Pinatubo event increased the stratospheric sulfur burden by a factor of 100 (Bluth et al., 1992).

Satellite observations from the Ozone Mapping and Profiler Suite (OMPS) Limb Profiler (LP) instrument, the Stratospheric Aerosol and Gas Experiment III (SAGE III) onboard the International Space Station (ISS), and Infrared Atmospheric Sounder Interferometer (IASI) observations can be used to derive aerosol properties, including extinction, effective radius, surface area density (SAD), and stratospheric optical depth (SAOD) (Duchamp et al., 2023; Taha et al., 2021; Taha et al., 2022; Bourassa et al., 2023; Schoeberl et al., 2024; Sellitto et al., 2024; Johnson et al., 2025). We also use the Global Space-based Stratospheric Aerosol Climatology (GloSSAC) combined observational dataset (Thomason et al., 2018; Kovilakam et al., 2020), which mostly consists of SAGE observations. Figure 7.1a (see also Chapter 3) shows the evolution of the 1020 nm global average (60°S–60°N) SAOD following the eruption from four sources: NASA OMPS-LP (Taha et al., 2021; Johnson et al., 2025); USask OMPS-LP (Bourassa et al., 2023); SAGE III/ISS (Thomason et al., 2018); and GloSSAC (Kovilakam et al., 2020).

For the NASA OMPS-LP data shown in Figure 7.1a, we use the latest Version 2.5 product (Johnson et al., 2025), replacing the Version 2.1 product used by Taha et al. (2022). In the new NASA OMPS-LP V2.5 algorithm, convergence was improved over V2.1 by significantly increasing the number of iterations to improve the retrieval performance. The short-wavelength aerosol profiles at 510, 600, 675, and 745 nm were filtered for unrealistic values (mostly at lower altitudes and large scattering angles) using the colour ratio relative to 869 nm. To eliminate unrealistic and anomalous retrievals, the aerosol profiles were also filtered for values greater than 0.1 km^{-1} and where the retrieval residual is greater than 50%. See Supplementary S2 (Figure S.II.3) for a detailed comparison of NASA OMPS-LP V2.5 and V2.1 SAODs.

We use the SAGE Ångström Exponent to convert the NASA and USask OMPS 745 nm SAODs to 1020 nm in order to compare them with the HTHH-MOC model output, which is available at this wavelength. Additionally, we present the original SAGE 1020 nm SAOD, GloSSAC, and the NASA OMPS 997 nm SAOD. Due to limited sampling, SAGE data smooth the initial rise in Hunga's SAOD, but they provide the most reliable observations 3–4 months after the eruption and serve as the foundation for the GloSSAC combined observational dataset.

Since our focus is on Hunga's impact on SAOD, we removed the background SAOD from all observed SAOD records by defining Hunga's SAOD as the increase over a 10-day average SAOD prior to the eruption. While this approach is not entirely precise, using a climatological background SAOD seasonal cycle would also be problematic because of interannual variability. Therefore, we opted for this method as the simplest and most easily reproducible.

Figure 7.1a compares SAOD estimates described above. The NASA OMPS-V2.5 1020 nm SAOD converted from 745 nm observations is unrealistically high. The NASA OMPS-V2.5 SAOD at 997 nm is in better agreement with the other sources. It reaches ~0.006 in one month after the eruption, while the USask OMPS SAOD is a factor of 1.5 smaller. The SAGE III/ISS SAOD and GloSSAC lie between the two OMPS estimates. The differences in the SAOD estimates between the various satellite retrieval algorithms can be viewed as uncertainty in the measurement.

All the measurements show a shift in SAOD from the tropics to the extratropical Southern Hemisphere (SH) during May–June 2022 (Schoeberl et al., 2023). Models capture the transport of the SA plume throughout the stratosphere reasonably well (see Chapter 3). The stratospheric SAs are removed from the stratosphere by gravitational sedimentation, mixing into the troposphere through tropopause folds, and transport to the troposphere in the polar regions (e.g., Kremser et al., 2016). The decay time for stratospheric sulfate aerosols depends on the latitude of the eruption (Toohey et al., 2025; Oman et al., 2006). According to observations, most of the Hunga aerosol loading had disappeared by the end of 2023 (Figure 7.1a; Schoeberl et al., 2024).

To depict Hunga's SAOD from the HTHH-MOC models, Figure 7.1b presents the difference between simulations with volcanic emissions and their corresponding control runs, thereby effectively removing the background SAOD. The models exhibit a range of results, with WACCM6MAM and GEOSCCM pro-

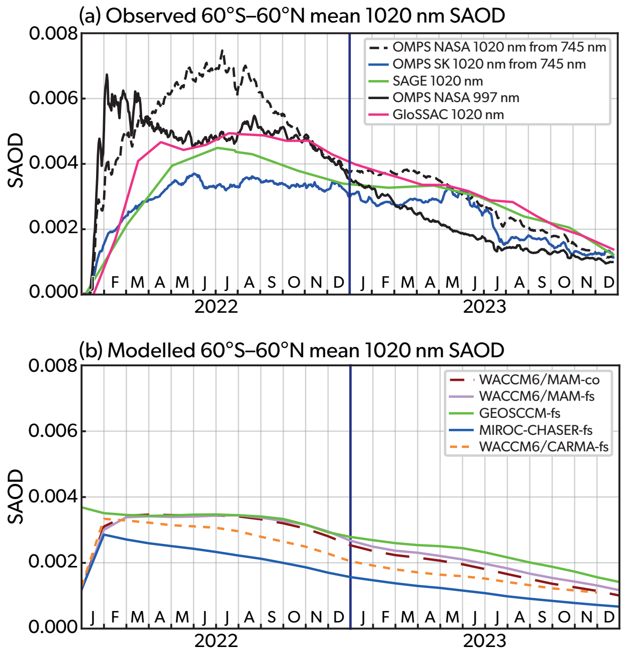

Figure 7.1: *Near-global average (60°S–60°N) Hunga SAOD for the first two years after the eruption, with background SAOD removed. (a)* Observational estimates: *NASA OMPS-LP-V2.5 at 1020 nm SAOD is derived by converting 745 nm SAOD using the SAGE III/ISS 745-to-1020 nm Ångström exponent. USask OMPS-LP 1020 nm SAOD is obtained in the same way. NASA OMPS-LP-V2.5 997 nm and SAGE III/ISS 1020 nm SAODs are shown directly, without conversion, along with GloSSAC 1020 nm. (b)* Model results: *Ensemble-mean Hunga – control SAODs from WACCM6MAM-co, WACCM6-MAM-fs, WACCM6CARMA-fs, MIROC-CHASER-fs, and GEOSCCM-fs ensembles.*

ducing the highest SAOD and MIROC-CHASER the lowest. Removing the background helps bring the model SAODs closer to the observations. Nevertheless, considering the spread in both observational and model data, the modelled SAODs are a factor of 1.3 to 2.0 lower than the observed SAOD. Assuming that the model reduced SAOD is due to smaller initial SO_2 injection, the corresponding adjusted SO_2 emission estimate would be 0.65–1.0 Tg. This higher SO_2 amount is consistent with more recent estimates reported by Stenchikov et al. (2025), Schoeberl et al. (2024), and Sellitto et al. (2024). The observational estimate of 0.7 Tg by Carn et al. (2022) lies at the lower bound of this range.

Hunga's SAOD is the largest in the observation record since the 1991 Pinatubo eruption (Khaykin et al., 2022). It was suggested that the Hunga eruption was approximately twice as effective at producing SAOD per unit mass of emitted SO_2 compared to similar or more significant eruptions like Raikoke, Calbuco, or Nabro (Sellitto et al., 2022; Taha et al., 2022); see Chapters 2 and 3 for further information. We attribute Hunga's relatively high SAOD to the fact that the volcanic materials were initially injected in the upper stratosphere and did not interact with the tropopause layer during their descent to the lower stratosphere (see Chapter 2). As a result, volcanic clouds did not lose SO_2 and SO_4 through the tropopause (Stenchikov et al., 2021; Stenchikov et al., 2025), which led to larger SAOD generation per unit mass of emitted SO_2. Stenchikov et al. (2025) demonstrated that Hunga's aerosol size enhanced SAOD per unit SO_2 mass by only 10–15% relative to Raikoke and Nabro. Thus, reconciling the simulated and observed SAOD requires assuming an SO_2 emission greater than 0.5 Tg.

7.2.2 *Hunga's water vapour perturbation*

The Hunga eruption injected WV directly into the upper stratosphere even reaching the lower mesosphere (Khaykin et al., 2022; Millán et al., 2022; Vömel et al., 2022). Satellite observations from the Aura Microwave Limb Sounder (MLS) revealed unprecedented stratospheric H_2O concentrations following the eruption (see Chapter 3). The amount of volcanic WV retained in the stratosphere after the eruption was unusually high, exceeding 120–130 Tg, which represents about a ~10–15% increase in the global stratospheric WV burden (Vömel et al., 2022; Millán et al., 2022; Millán et al., 2024; Santee et al., 2023). As a result, the 2022 Hunga eruption sparked considerable debate about its climate effect.

Hunga's WV cloud initially formed over the volcano at (175° W; 20°S) and spread throughout the tropics south of the equator. Millán et al. (2024) detailed the evolution of the WV anomaly using MLS observations. Models reproduce the transport of the WV cloud throughout the stratosphere reasonably well (see Chapter 3). The large injection of water vapour has the potential to alter stratospheric chemistry and circulation (Coy et al., 2022; Chen et al., 2023; Fleming et al., 2024; Niemeier et al., 2023; Maycock and Shine, 2012) and might indirectly impact other radiatively active gases, like ozone and methane, and the tropospheric climate.

The WV plume initially descended from 30–40 km to 25–27 km, then slowly ascended over the following year, reaching mesospheric altitudes (>50 km) during 2023–2024 (see Chapters 2 and 3; Sellitto et al., 2022; Nedoluha et al., 2024; Millán et al., 2024; Wallis et al., 2025; Randel et al., 2023; Niemeier et al., 2023). This initial plume descent was not seen in SAGE III/ISS

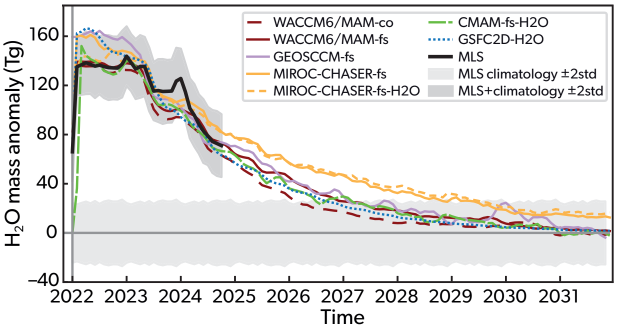

Figure 7.2: *Perturbation of the global stratospheric water vapour burden (Tg) observed by MLS (black) and simulated using several chemistry-climate models, as indicated in the legend. The light-gray shading indicates the 2σ variability range of the MLS observations calculated using data from 2005-2021, while the dark-gray shading represents 2σ variability over the MLS observational record for the 2022-2025 period. (Adapted from Zhuo et al., 2025.)*

observations, because SAGE III/ISS missed the initial stage of the plume evolution. In the model simulations (Chapter 3, e.g., WACCM6MAM) the descent phase is short-lived, as WV and SO_2 were released near 30 km, just above the level where the plume descent halted. The excess Hunga WV will ultimately return to the troposphere at mid-high latitudes via the BDC (Holton et al., 1995; Appenzeller et al., 1996) and by sedimentation of polar stratospheric cloud (PSC) ice crystals in the Antarctic polar vortex (see, e.g., Kelly et al., 1989; Fahey et al., 1990; Vömel et al., 1995; Nedoluha et al., 2002; Zhou et al., 2024).

Given the multiyear stratospheric lifetime for trace gas anomalies, the Hunga WV will have a multi-year impact. The HTHH-MOC simulations suggest that stratospheric WV will take 4–7 years to return to pre-eruption levels (Figure 7.2, see also Chapter 3). Based on model simulations, Fleming et al. (2024) and Zhou et al. (2024) suggested a ~2.5–4-year decay timescale for the Hunga water vapour anomaly, and Schoeberl et al. (2025) found that Hunga's WV lifetime is ~3.7 years, which is consistent with the HTHH-MOC's model results (Figure 7.2). MLS observations suggest a significantly longer e-folding decay timescale of 12.2 years (Millán et al., 2024). This discrepancy might be partly caused by the shorter water vapour record used by Millán et al. (2024), and how the MLS residence time was calculated (Schoeberl et al., 2025; Toohey et al., 2025).

7.2.3 *Hunga's ozone perturbation*

Wang et al. (2023) and Wilmouth et al. (2023) used models and observations to show that for a few months after the Hunga eruption in the SH tropics ozone mixing ratio increased in the upper and middle stratosphere but decreased in the lower stratosphere. The amplitude of ozone changes was within natural variability. The aerosol and water vapour anomalies can affect stratospheric dynamics and chemistry, resulting in detectable effects on atmospheric radiation and potentially the surface climate (Muthers et al., 2015; Wang et al., 2013; Fleming et al., 2024). The added stratospheric radiative cooling from the water vapour injection set up a secondary circulation (Coy et al., 2022) that lifted the ozone layer at southern mid-latitudes near 25 km. This decreased the mid-latitude ozone concentration in the 20–25 km layer by transporting lower concentration ozone upward. MLS also detected enhanced ClO (Santee et al., 2023) due to heterogeneous chemistry on aerosols. Relative to the climatology, the ozone perturbations in the stratosphere are within 2–3% and in the mesosphere 5–6%. However, the absolute changes in ozone content in the mesosphere are minor because of low background concentration (Santee et al., 2023; Schoeberl et al., 2024). After 2023, ozone losses in the tropics remain modest (<10 DU).

7.3 Hunga's radiative forcing

RF refers to the perturbation of the radiative energy flux at TOA, tropopause (TROP), and surface (SURF) caused by radiatively active agents of interest. RF at TOA measures the energy imbalance at the boundary of the Earth's climate system and is predictive of the global mean temperature impact of a particular radiative agent (Ramaswamy et al., 2019). The forcing at the tropopause integrates the change in the energy balance of the troposphere-surface system. RF at SURF is indicative of the radiative heating or cooling of the land and ocean. Ocean heating/cooling induced by volcanic RF initiates long-term climate changes that can persist for several decades after the volcanic event (Stenchikov et al., 2009; Delworth et al., 2006). Table 7.1 defines some standard terms used in this chapter.

7.3.1 *IRF, ERF, and SARF*

Depending on the methods, RF can be categorised as Instantaneous Radiative Forcing (IRF), stratosphere-adjusted radiative forcing (SARF), or effective radiative forcing (ERF) (Hansen et al., 2005; Ramaswamy et al., 2019; Andrews et al., 2021). IRF is defined as the radiation perturbation caused by the change in the radiative agent of interest when no other changes to the atmosphere-surface system are allowed. IRF can be calculated using radiative transfer models (Sellitto et al., 2022; Jenkins et al., 2023; Stenchikov et al., 2025; Yu and Huang, 2024) following the partial radiative perturbation concept (Wetherald and Manabe, 1988) without accounting for atmospheric adjustments. IRF is also often evaluated using empirical formulas or scaling relations (Hansen et al., 2005; Larson and Portmann, 2016; Yu et al., 2023b; Schoeberl et al., 2023; Schoeberl et al., 2024; Marshall et al., 2020). Column stand-alone radiative-transfer models driven by observed meteorology and atmospheric composition are well suited for evaluating IRF. IRF calculations are also implemented in regional and global climate models by a "double call" of radiative routines (Stenchikov et al., 1998). The double-call approach computes radiative fluxes twice, once with and once without the optically active constituents of interest, using the same meteorological profiles, and defines the IRF as the difference between the two.

Unfortunately, a double-call capability is not implemented in most of the HTHH-MOC models. Instead, they calculated IRF in the runs with nudged meteorology as a difference of radiative fluxes in perturbed and control experiments. SA+WV IRF was calculated using the nudged meteorology ensemble with SA and WV emissions. WV IRF was calculated in the nudged meteorology runs with only WV emission. SA IRF was calculated in the experiments with nudged meteorology and only SO_2 emissions. Because nudging suppresses variability in meteorological fields, it typically excludes the stratospheric temperature adjustment. However, the clear-sky SA+WV, SA, and WV IRFs still inherently reflect the influence of non-nudged variables that affect radiative fluxes – such as ozone perturbations and changes in PSCs. This must be kept in mind when interpreting the IRFs obtained with HTHH-MOC models.

Subsequent to the introduction of IRF, stratospheric temperature adjustment was recognised as an essential process influencing the RF magnitude, leading to the definition of SARF, which is often quantified by the Fixed Dynamical Heating method (Fels et al., 1980). SARF does not include any tropospheric adjustments or other stratospheric adjustments than temperature. For stratospheric water vapour perturbations in the middle and upper stratosphere, IRF at the tropopause usually closely matches the SARF at the tropopause (Jenkins et al., 2023; Solomon et al., 2010).

Recently, it has been recognised that fast tropospheric adjustments can also play an important role for radiative forcing (Sherwood et al., 2015). This finding led to the introduction of ERF, which accounts for both stratospheric and tropospheric adjustments. In many forcing cases (e.g., carbon dioxide), ERF is a better predictor of eventual global mean surface air temperature change than IRF (Hansen et al., 2005; Smith et al., 2020; Andrews et al., 2021). For example, some studies have suggested that cloud adjustment in the troposphere can add an essential modification to the radiative effect of stratospheric water vapour (Huang et al., 2020; Li and Newman, 2020; Wang and Huang, 2024; He and Huang, 2025). In the HTHH-MOC experiments, ERF is calculated as the difference in radiative fluxes between perturbed (with radiatively active agents) and control (without radiatively active agents) runs with prescribed sea surface temperatures (SST). We note that this diagnosis of ERF includes chemical adjustments, e.g., via stratospheric ozone, as well as physical adjustments.

Short-wave IRF, SARF, and ERF are largely independent of changes in environmental temperature, and as a result, their values are similar. In contrast, longwave SARF and ERF differ from the LW IRF because they are influenced by changes in atmospheric temperature, whereas the LW IRF is not (Forster et al., 2016).

7.3.2 Clear sky and all sky RF

RF can be calculated for all-sky or clear-sky conditions. The all-sky RF provides a better estimate of the global average surface temperature response. For example, Wang and Huang (2024) showed that cloud feedback in their model tends to reduce the SW radiative impact of the Hunga volcanic cloud. However, clear-sky forcing is a more meaningful metric than all-sky forcing for characterising the evolution of a volcanic cloud and comparing model performance, as cloud parametrisations vary significantly across models. We must emphasise that an all-sky forcing is acting within the models, i.e., an all-sky forcing drives the simulated climate responses in the HTHH-MOC ensembles.

Using observed distributions of WV and SA, we can calculate the 2022-2024 radiative forcing and compare it with available ground-based observations and satellite retrievals (Schoeberl et al., 2022; Schoeberl et al., 2023; Schoeberl et al., 2024; Sellitto et al., 2022;

Table 7.1: *Radiative Forcing Terminology.*

Acronym	Term	Definition
IRF	Instantaneous Radiative Forcing	Radiation perturbation at TOA, TROP, or SURF caused by the change in the radiative constituents alone.
ERF	Effective Radiative Forcing	A difference in corresponding radiative fluxes between perturbed and unperturbed experiments with prescribed SST which allow for radiative adjustments in the atmosphere and by the land surface.
SARF	Stratosphere-adjusted Radiative Forcing	Radiative forcing that accounts only for stratospheric temperature adjustment.
TOA	Top of Atmosphere	The model's top level.
TROP	Tropopause	The tropopause level, e.g., 100 hPa.
SURF	Surface	Surface level.

Sicard et al., 2025; Gupta et al., 2025). Beyond 2024, we must rely on models to estimate the RF. To increase the model's credibility, we use the observations to validate models for the 2022-2024 period. To calculate Hunga's radiative impact, we must account for the effects of stratospheric SA, WV, and changes to other radiatively active constituents, e.g., stratospheric ozone.

7.3.3 Hunga's sulfate aerosol and water vapour IRF

The radiative impact of volcanic aerosols is well-known (e.g., Ramaswamy et al., 2019; Kremser et al., 2016; Stenchikov et al., 1998). They cool the surface–troposphere system by reducing downwelling solar radiation, while simultaneously causing warming within the stratospheric aerosol layer due to absorption of solar NIR and terrestrial LW radiation. As noted in Section 7.2.1, Hunga's SO_2 injection is small compared to climatologically significant eruptions like the 1991 Pinatubo event. The SO_2-to-SO_4 conversion rate in the Hunga plume appears to be 1-2 weeks due to the enhanced WV mixing ratio (see Chapter 3). This is 2-3 times faster than in all previously observed eruptions (Carn et al., 2016). After the major Hunga eruption pulse on 15 January 2022, the SAOD increased during a few weeks after the eruption due to the rising of the SO_4 mass and particle coagulation and condensation growth (Zhu et al., 2022), which led to local IRF values reaching nearly -2.0 W m^{-2} in some locations (Sellitto et al., 2022; Sicard et al., 2025), and a global averaged IRF of -0.5 W m^{-2} through the first year (Schoeberl et al., 2023; Stenchikov et al., 2025). The LW SA IRF is positive at the TOA, SURF, and the TROP, but SW SA IRF is negative at all atmospheric levels. The absolute value of SA SW IRF is approximately five times larger than that of SA LW IRF, i.e., the net IRF due to Hunga SA is negative at all levels.

Figure 7.3 presents the all-sky and clear-sky net IRFs averaged over 0-60°S at the TOA, TROP, and SURF, calculated using the WACCM6MAM-nd ensemble with nudged meteorological fields (see Supplementary S1 for more information about HTHH-MOC). The all-sky SA+WV and SA IRFs are approximately 20–30% smaller than their clear-sky counterparts. The all-sky IRF exhibits stronger temporal changes than the clear-sky IRF due to cloud variability (Figure 7.3). The near-hemispheric (0-60°S) average clear-sky SA+WV net IRFs at TOA, TROP, and SURF generally follow the SA net IRF, averaging around -0.5 W m^{-2} over 2022-2023. The increase in SA IRF magnitude during the austral summer of 2022-2023 is attributed to the poleward spread of SA into southern mid- and high latitudes and the seasonal rise in solar insolation. As previously noted, the IRFs in Figure 7.3 are based on the simulations with a 0.5 Tg SO_2 emission. To match the observed SAOD the models would likely have to increase SO_2 emissions by a factor of 1.3-2.0. With this adjustment and considering that Figure 7.3 shows the 0–60°S average rather than global IRF, the HTHH-MOC results are consistent with findings from Schoeberl et al. (2024), Stenchikov et al. (2025) and Gupta et al. (2025).

The clear-sky WV net IRF at TOA in the WACCM6-MAM-nd run with nudged meteorology is negative in 2022, but counter-intuitively becomes slightly positive in 2023 (Figure 7.3a). This may be due to changes in ozone or PSCs, as the method used by the HTHH-MOC models to calculate IRF does not isolate or remove the effects of ozone and PSCs. The HTHH-MOC WV IRF is broadly consistent with other estimates of WV IRF (Stenchikov et al., 2025; Wang and Huang, 2024). The SW WV IRF is caused by WV NIR absorption and is at least one order of magnitude smaller than the LW WV IRF. Although it is included in all calculations, its contribution appears negligible. Stenchikov et al. (2025) and Wang and Huang (2024) calculated the WV IRF using climate models and reported consistent WV IRFs at TOA of the order −0.05 W m^{-2}.

After the first 5-6 months following the injection, Hunga's WV layer tends to ascend in the stratosphere and thus has a longer stratospheric residence time (4-7 years) than SA (see Figures 7.1 and 7.2). SA and WV radiative impacts counteract each other for about 2 years when Hunga's SAs are present in the stratosphere. In contrast to SA, which warms the stratosphere and cools the troposphere, stratospheric WV cools the stratosphere and warms the troposphere (Forster and Shine, 1999; Solomon et al., 2010; Dessler et al., 2013). The SA RF<0 prevails during the first 2 years (Schoeberl et al., 2024; Stenchikov et al., 2025; Gupta et al., 2025). After 2 years, only Hunga WV RF>0 matters, which could potentially warm the climate (Jenkins et al., 2023; Jucker et al., 2024; Wang and Huang, 2024), even though, as assessed in this Chapter, that impact is likely to be undetectable.

The stratospheric WV layer absorbs upward LW flux, attenuating the outgoing LW irradiance above the WV layer. However, it also increases upward LW flux from local emission, compensating for this attenuation. As a result, WV LW RF at TOA remains minimal, while heating rates within the WV layer reach −0.2 K/day, causing cooling in the stratosphere (Chapter 4; Stenchikov et al., 2025). Riese et al. (2012) show that a stratospheric WV layer below 20 hPa causes a positive IRF, while a WV layer above 20 hPa causes a negative IRF. However, whether there is overall heating or cooling of the Earth's surface strongly depends on the water vapour's vertical (and perhaps horizontal) distribution and stratospheric temperature adjustment. These factors deserve further consideration.

7.3.4 Empirically calculated ERF

Schoeberl et al. (2024) computed the clear-sky SA ERF (Figure 7.4) using observed aerosol extinction and a parametrisation similar to Yu et al. (2023a), Yu and Huang (2023) and Yu et al. (2023b). In Figure 7.4, the total forcing along with the various forcing components are shown. Figures 7.4a, b show the net forcing computed using the NASA and USask OMPS aerosol SAOD estimates. The SA forcing is confined mainly to the Southern Hemisphere low- and mid-latitudes (see Figure 7.4a, b, Stenchikov et al., 2025; Schoeberl et al., 2023; Schoeberl et al., 2024). The clear-sky net ERF calculated using NASA OMPS-LP-V2.1 SAOD exceeds −1 W/m^2 in the tropics, while the ERF calculated using the USask SAOD retrievals is about half that amount. The components of ERF from various optically active agents are shown at the equator, 20°S, and 40°S, illustrating their evolution over time. The black line is the net total ERF. The SW SA forcing component is in red. As the aerosol disperses and sediments out of the stratosphere, its radiative forcing becomes negligible by the end of 2023. The SA loading, initially highest in the tropics at the beginning of 2022, shifts to the southern extra-tropics by the end of 2022. NIR absorption by WV (yellow-green) is much weaker than its LW emission (green). The WV LW flux increases the TROP ERF, whereas the NIR absorption by WV reduces it. Finally, the changes in LW flux due to stratospheric temperature changes (dark blue) also modify the net flux. The temperature anomalies are the observed 2022-2023 differences from the 10-year climatology. These anomalies reflect some natural variability and therefore do not provide a clean estimate of the temperature adjustment contribution to the ERF. The impact of natural temperature variability, which is highest in the extra-tropics, can be seen toward the end of 2023, where all the other radiative anomalies have diminished.

The secondary circulation set up by the water vapour radiative cooling in the stratosphere causes a decrease in column ozone in mid-to-late 2022 (Wang et al., 2023; Wilmouth et al., 2023). The ozone decrease could be partially caused by changes in planetary wave propagation and the BDC driven by the Hunga volcanic (WV+SA) forcing (Yu et al., 2023b). Ozone depletion causes increases in the SW downward flux at TROP and SURF, partly compensating for aerosol dimming. Schoeberl et al. (2024) computed ozone IRF directly from observed changes in stratospheric ozone (see Figure 7.4), which is surprisingly large. The stratospheric ozone reduction increases the solar flux, even though the ozone reduction is modest (orange line). Ozone LW flux (blue-green) changes are small and are included here only for completeness. It should be noted that the ozone ERF estimate presented here represents an upper bound, as it does not account for the attenuation of tropical UV flux by the Hunga aerosol layer. The ozone ERF is significantly smaller than the SA IRF.

7.3.5 Model calculated ERF

On average, the stratospheric net IRF driven by WV (and ozone) is small compared to the aerosol net IRF.

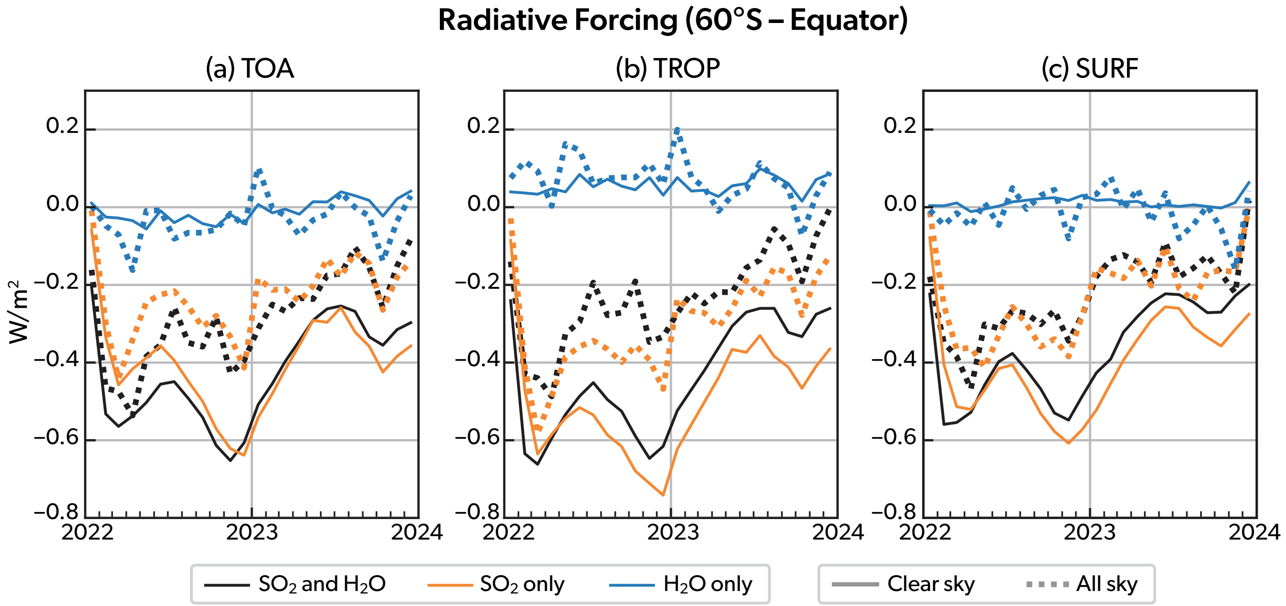

Figure 7.3: *All-sky (dotted curves) and clear-sky (solid curves) (0-60°S) average net SA+WV, WV, and SA IRFs (W m^{-2}) from the WACCM6MAM-nd run with nudged meteorology: (a) at TOA; (b) at TROP; (c) at SURF. (Adapted from Quaglia et al., 2025.)*

During the first two years, the WV and ozone IRFs were overwhelmed by a negative SA IRF, so the net global IRF at all levels was about −0.4±0.1 W m^{-2} (Schoeberl et al., 2024; Stenchikov et al., 2025). This is also found for ERF. Unlike IRF, the ERF cannot be calculated simultaneously for the SA and WV in a climate model in one run (Stenchikov et al., 2025). However, the SW components of IRF and ERF are similar at all levels. The LW ERF might differ from the LW IRF due to, e.g., stratospheric temperature adjustment. For example, the LW WV ERF at TOA has a different sign (positive) than the LW WV IRF (negative).

Stenchikov et al. (2025) calculated LW and SW WV and SA ERF, combining results from the different experiments (SA+WV and WV only) with a regional climate model, WRF-Chem, that interactively calculated the spatial-temporal distribution of volcanic plume, SAOD, and temperature responses. Wang and Huang (2024) calculated WV ERF assuming a prescribed WV perturbation in the 50-10 hPa layer using the FDH method (Fels et al., 1980). Despite different approaches, globally averaged WV ERF from Stenchikov et al. (2025) and WV ERF from Wang and Huang (2024) are consistent with each other, amounting to 0.05 W m^{-2}.

In the HTHH-MOC, SA+WV ERF is obtained from the prescribed ocean WACCM6MAM-fs ensemble, with SO_2 and WV emissions. Long-term integrated effects can be determined by computing an integrated average $\overline{ERF}$ defined as

$$\overline{ERF}(t) = \frac{1}{t} \times \int_0^t ERF(t')dt' \qquad (7.1)$$

To evaluate the long-term radiative impact of the Hunga plume, we plot in Figure 7.5 the (0-60°S) average clear-sky net time integrated ensemble mean SA+WV net $\overline{ERF}$. We also show $\overline{IRF}$

$$\overline{IRF}(t) = \frac{1}{t} \times \int_0^t IRF(t')dt' \qquad (7.2)$$

calculated within the run with nudged meteorology, WACCM6MAM-nd, and $\overline{RF}$ calculated as (Hunga-control) within the WACCM6MAM-co ensemble with coupled ocean using a similar operator:

$$\overline{RF}(t) = \frac{1}{t} \times \int_0^t RF(t')dt' \qquad (7.3)$$

In Figures 7.5a, b, c we present net $\overline{ERF}$, $\overline{IRF}$, and $\overline{RF}$ at the TOA, TROP, and SURF, respectively. At each time, $\overline{ERF}$ (as well as $\overline{IRF}$ and $\overline{RF}$) is equal to the average forcing for all previous periods starting from the time of the Hunga eruption. $\overline{ERF}$ is much smoother than the instantaneous (0-60°S) averaged ERF and is a more precise metric of the perturbation of the energy balance of the climate system. Increased stratospheric WV tends to warm the climate system on average, but SA cooling prevails for the entire simulation period.

(a) Net forcing, NASA OMPS

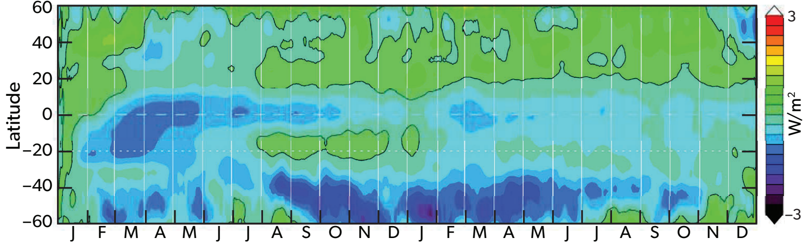

(b) Net forcing, USask OMPS

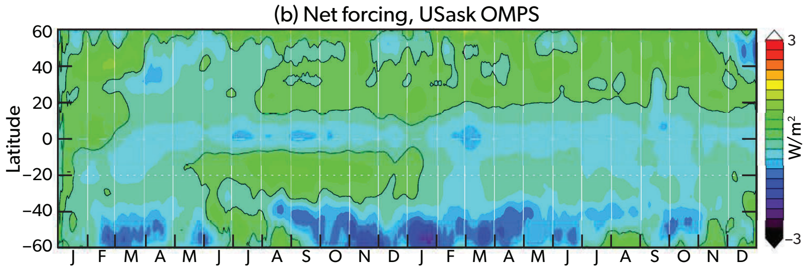

(c) Tropopause fluxes at the Equator, NASA OMPS

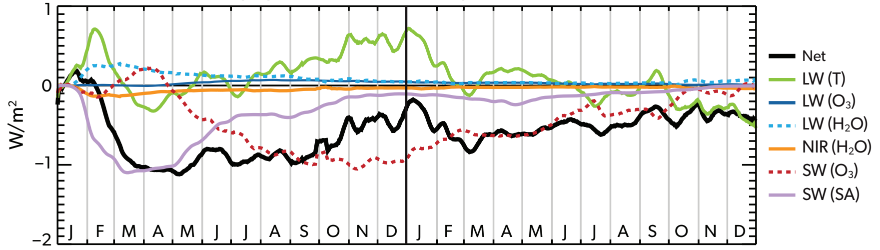

(d) Tropopause fluxes at 20°S, NASA OMPS

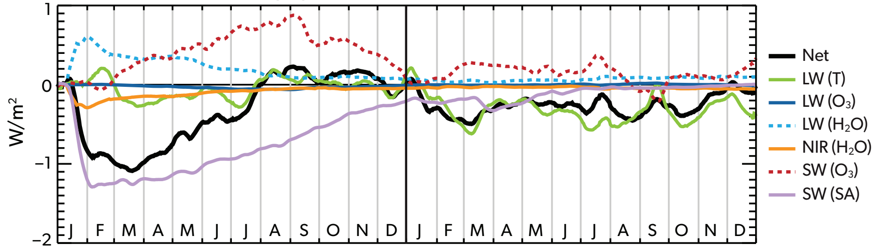

(e) Tropopause fluxes at 40°S, NASA OMPS

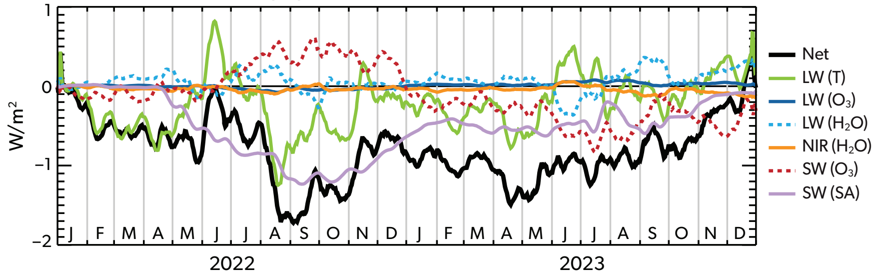

Figure 7.4: *Hunga's clear-sky empirically calculated ERF at the TROP: (a) Using SAOD obtained by the NASA OMPS-LP-V2.1 algorithm (Taha et al., 2021; Taha et al., 2022) and (b) Using SAOD obtained by the USask algorithm (Bourassa et al., 2023), which has a smaller estimated SAOD. Panels (c, d, e) show the various radiative forcing components of TOA's ERF as labelled in the legend at the Equator, 20°S, and 40°S. (Adapted from Schoeberl et al., 2024, reproduced with permission.)*

In 2023, the $\overline{\mathrm{IRF}}$ (calculated within the run with nudged meteorology, WACCM6MAM-nd) reaches −0.5 W m^{-2} at the TOA, −0.55 W m^{-2} at the tropopause, and −0.45 W m^{-2} at the surface, with values around −0.4 W m^{-2} at all levels in 2024. The $\overline{\mathrm{ERF}}$ (calculated within the ensemble with prescribed ocean, WACCM6MAM-fs) is slightly weaker, reaching −0.3 W m^{-2}, −0.45 W m^{-2}, and −0.4 W m^{-2} at TOA, TROP, and SURF, respectively. The $\overline{\mathrm{RF}}$ (calculated within the ensemble with coupled ocean, WACCM6MAM-co) closely tracks $\overline{\mathrm{ERF}}$ during the first two years following the eruption.

In 2030, $\overline{\mathrm{ERF}}$ is still of the order of −0.1 W m^{-2}, indicating the decadal-average cooling effect of the Hunga eruption. Two years after the eruption, $\overline{\mathrm{ERF}}$ at TOA equals −0.3 W m^{-2}, while $\overline{\mathrm{IRF}}$ equals −0.4 W m^{-2}. This is consistent (assuming an increase of SO_2 emission by a factor of 1.3-2.0, as discussed above) with other estimates made using observations and different models (Schoeberl et al., 2024; Stenchikov et al., 2025; Gupta et al., 2025).

7.3.6 Uncertainty in radiative forcing

Discrepancies among the various estimates of the radiative forcing of Hunga primarily stem from uncertainties in the amount of injected SO_2 (Carn et al., 2022; Sellitto et al., 2024) and in the measurements of SAOD (Figure 7.1a, Taha et al., 2022; Bourassa et al., 2023; Schoeberl et al., 2024). Models may also introduce inconsistencies due to differences in their representations of SA and WV transformation processes and transport. The abundance of WV affects stratospheric temperature, chemistry, and dynamics, as described in 4 and 5, with the potential to indirectly influence the planet's radiative balance. These processes are technically included in the HTHH-MOC, but the ability of the model to quantitatively simulate these indirect effects remains a challenge.

The RFs calculated with the same model but in different experiments also could differ. The net SA+WV IRF calculated from the WACCM6MAM-nd run with nudged meteorology, ERF calculated using the WACCM6MAM-fs ensemble with prescribed SST, and RF calculated using the WACCM6MAM-co ensemble with coupled ocean are shown in Figure 7.6 at TOA, TROP, and SURF. The difference between the RFs appears to be about 10–20%.

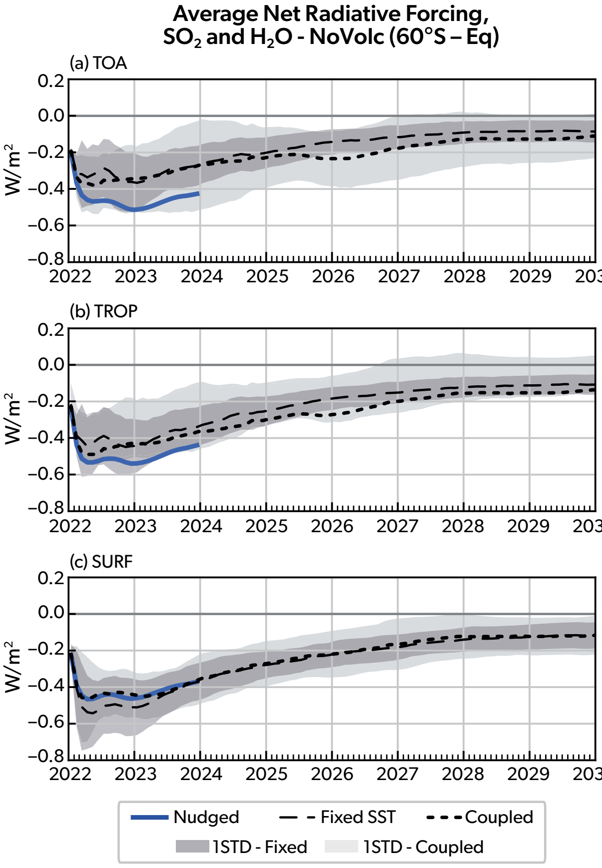

Figure 7.5: *Near-hemispheric (0–60°S) average clear-sky net ensemble-mean Hunga $\overline{\mathrm{ERF}}$ from the WACCM6MAM-fs prescribed-ocean ensembles, $\overline{\mathrm{IRF}}$ from the WACCM6MAM-nd run with nudged meteorology, and $\overline{\mathrm{RF}}$ from the WACCM6MAM-co coupled-ocean ensemble: (a) at TOA; (b) at TROP; (c) at SURF. (Adapted from Quaglia et al., 2025.)*

However, the uncertainties in clear-sky IRFs calculated in four different models (Figure 7.7) reach 50% at TOA and TROP and are slightly smaller at SURF. These models all use nudged meteorology so that temperature differences are minimised. Thus, the discrepancies in IRF are only due to model differences in radiatively active constituents and radiative transfer parametrisations (ozone, H_2O, aerosols, PSCs), with aerosol differences being the dominant contribution. The uncertainty between the models is likely driven by the differences in the aerosol microphysics parametrisations, as the most significant IRF differences are seen between the models with different aerosol microphysics. The net IRF is highest in WACCM6MAM, which uses mode microphysics (Mills et al., 2016). In contrast, WACCM6CARMA, which employs bin microphysics (Tilmes et al., 2023), produces a net IRF that is roughly half as strong as that of WACCM6MAM. Finally, calculating RF for WV using broadband radiative transfer models (used in all climate models) could also be associated with a 30% computational error (Maycock and Shine, 2012; Forster et al., 2011; Stenchikov et al., 2025). However, this computational uncertainty is likely not critical, as the WV IRF is relatively small compared to the SA IRF during 2022–2024.

7.4 Hunga's climate impact

The impact of the Hunga eruption on tropospheric climate has been assessed using energy balance models (EBM) (e.g., Jenkins et al., 2023; Zhang et al., 2022), statistical relationships from past volcanic events (e.g., Schoeberl et al., 2024), or by scaling based on historical eruptions like Pinatubo in 1991 (Stenchikov et al., 2025). Clear-sky and all-sky RF are effective scaling predictors, producing comparable estimates for the Hunga eruption. From this perspective, Hunga's clear-sky SA + WV net RF is almost one order of magnitude smaller (in absolute value) than the clear-sky net SA RF generated by the 1991 Pinatubo eruption (-3.5 W/m^2; Stenchikov et al., 1998). Consistently, the maximum global mean surface temperature change in response to the Hunga eruption is expected to be about 10 times smaller than that caused by the Pinatubo eruption (Santer et al., 2001; Stenchikov et al., 2009), i.e., of the order of 0.05 K.

Climate models are more advanced tools (compared to EBMs and scaling) for assessing climate impacts. However, the internal variability in climate models can complicate the interpretation of climate responses to external forcing, especially when the forcing is small. Several studies have utilised climate models to evaluate the impact of the Hunga eruption (Zhu et al., 2022; Jucker et al., 2024; Stenchikov et al., 2025; Kuchar et al., 2025; Yook et al., 2025; Zhuo et al., 2025; Bednarz et al., 2025). Challenges arise due to the small response magnitude and RF uncertainties, complicating interpretation of the results. Here we show output from the HTHH-MOC ensemble runs (see Supplementary S3), which provide standardised simulations of the climate consequences of the Hunga eruption.

Section 7.3 describes Hunga's RFs, revealing that in the first two years following the eruption (2022–2023), SA RF dominates over the WV RF. After 2024, however, the SA RF decreases, so that the impacts of perturbations in WV and ozone become dominant. Accordingly, we divide our analysis of tropospheric climate changes into two phases: (1) the period when direct SA RF primarily drives climate perturbations (2022–2023) and (2) the period when only direct WV RF remains (2024–2031). It has been suggested (Kuchar et al., 2025; Stenchikov et al., 2025; Bednarz et al., 2025) that the direct WV radiative effect may be complicated by secondary effects resulting from the substantial chemical and dynamic feedbacks to perturbations of temperature, chemical composition, and circulation in the stratosphere caused by the Hunga eruption. If these stratospheric changes influence the troposphere, they could lead to longer-term tropospheric impacts. Therefore, we dedicate a separate section to examining tropospheric perturbations, focusing on stratosphere-troposphere dynamic interactions in high latitudes of both hemispheres and the role of stratospheric ozone changes.

7.4.1 SA-dominated climate response (2022-2023)

A detailed comparison of the models in the HTHH-MOC collection is provided in Supplementary S3 and in Zhuo et al. (2025). Here, we show the output from the WACCM6MAM ensemble, which exhibits the largest (in absolute value) IRF (see Figure 7.7), to explore the physical aspects of the response while utilising results from multiple models to assess the spread of outcomes, which we interpret as an uncertainty range.

First, we tested the global average surface air temperature (SAT) response to Hunga's RF (see Figure 7.8). We analyse the ensemble mean SAT perturbations ΔSAT calculated as the difference between perturbed WACCM6MAM-co (with coupled ocean model) and WACCM6MAM-fs (with prescribed SSTs) runs with SO_2 and WV emissions, and the corresponding control ensemble WACCM6MAM (without volcanic emissions).

We consider ΔSAT averages over land (ΔSAT_L), over the ocean (ΔSAT_O), and globally (ΔSAT_G). In the WACCM6MAM-co ensemble, ΔSAT_L is three times as large compared to ΔSAT_O, but hardly exceeds two SAT standard deviations in the control ensemble without volcanic injections during the 2022–2023 period. In other words, Hunga's climate impact remains barely distinguishable from natural internal variability, even when averaged over the 30-member ensemble. In the WACCM6MAM-fs ensemble with prescribed SSTs, the ΔSAT variability lacks the low-frequency oscillation induced by the perturbation of the ocean's ENSO cycle.

To reduce the SAT variability, we introduce an integrated time-dependent average $\overline{\Delta SAT}$

$$\overline{\Delta SAT}(t) = \frac{1}{t} \times \int_0^t \Delta SAT(t')dt' \qquad (7.4)$$

$\overline{\Delta SAT}$ represents the average of ΔSAT over a given

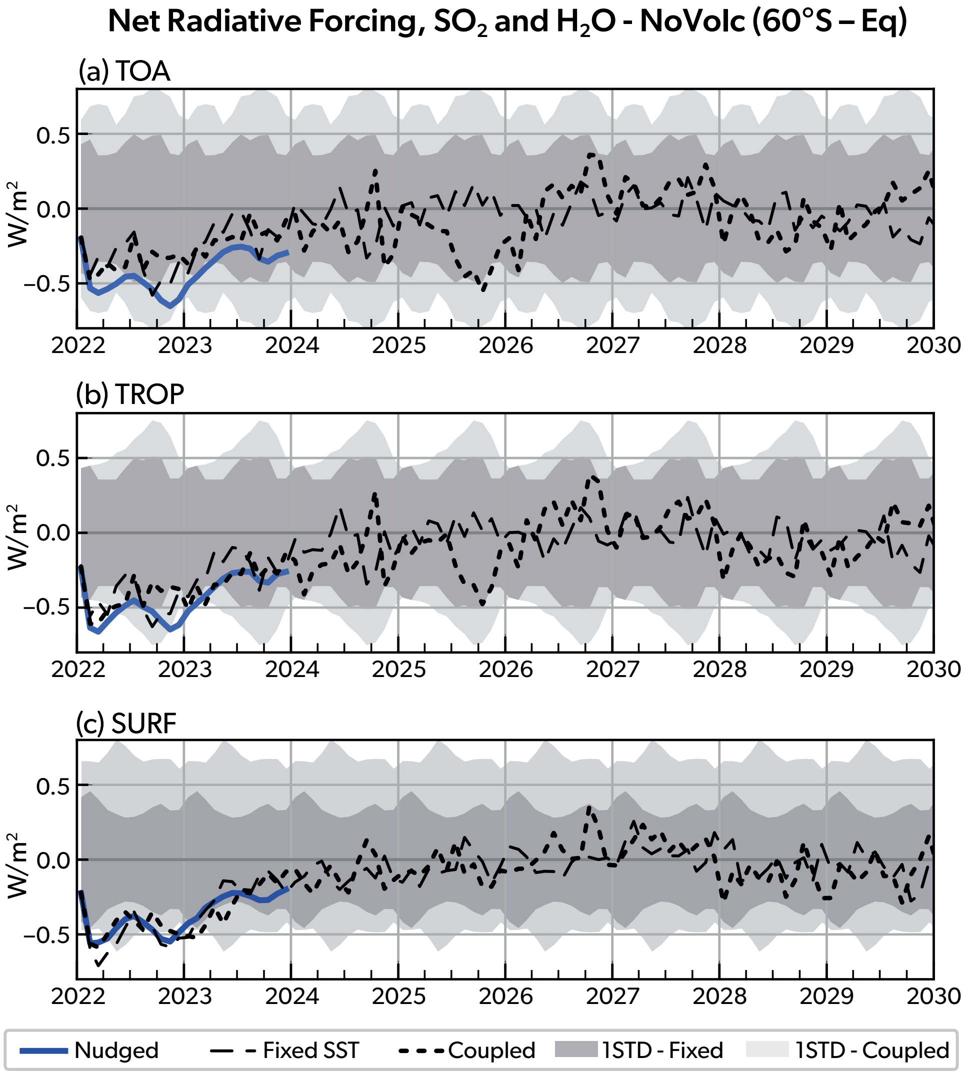

Figure 7.6: *Near-hemispheric (0-60°S) SA+WV clear-sky RFs (W m^{-2}) from the WACCM6MAM-nd run with nudged meteorology, the WACCM6MAM-co ensembles with coupled ocean, and the WACCM6MAM-fs ensembles with prescribed SSTs, shown at (a) TOA, (b) TROP, and (c) SURF. Dark shading indicates the one-standard-deviation range for WACCM6MAM-fs, while light shading indicates the one-standard-deviation range for WACCM6MAM-co. (Adapted from Quaglia et al., 2025.)*

time period starting from the Hunga eruption. $\overline{\Delta SAT}$ over land ($\overline{\Delta SAT_L}$), ocean ($\overline{\Delta SAT_O}$), and global ($\overline{\Delta SAT_G}$) areas are shown in Table 7.2. As expected, $\overline{\Delta SAT}_L$ in the coupled-ocean runs is almost three times larger than $\overline{\Delta SAT}_O$. An interactive ocean adds to the low-frequency variability (with ~3-year periodicity) in ΔSAT. The global accumulated cooling is largest at two years past the eruption, reaching −0.0303 K. This agrees with the −0.05 K cooling estimate obtained by scaling the Pinatubo SAT perturbation (Stenchikov et al., 2025). This magnitude of cooling is also consistent with other estimates (Zhang et al., 2022; Schoeberl et al., 2023). Such a slight temperature change would not be detectable above internal variability (see Figure 7.8).

The $\overline{\Delta SAT}$ in the WACCM6MAM-fs ensemble with prescribed SST is presented in Table 7.3. It also shows a generally small cooling response. However, the variability of the response indicates that the effect of natural variability is significant. For example, $\overline{\Delta SAT}$ over the ocean is positive (while RF < 0) during the first year, indicating that internal variability exceeds the forced signal. However, the 10-year average global mean $\overline{\Delta SAT}_G$ is negative and consistent between the coupled-ocean and fixed-SST ensembles. As expected, $\overline{\Delta SAT}_L$ in the coupled-ocean runs is almost three times larger than $\overline{\Delta SAT}_O$.

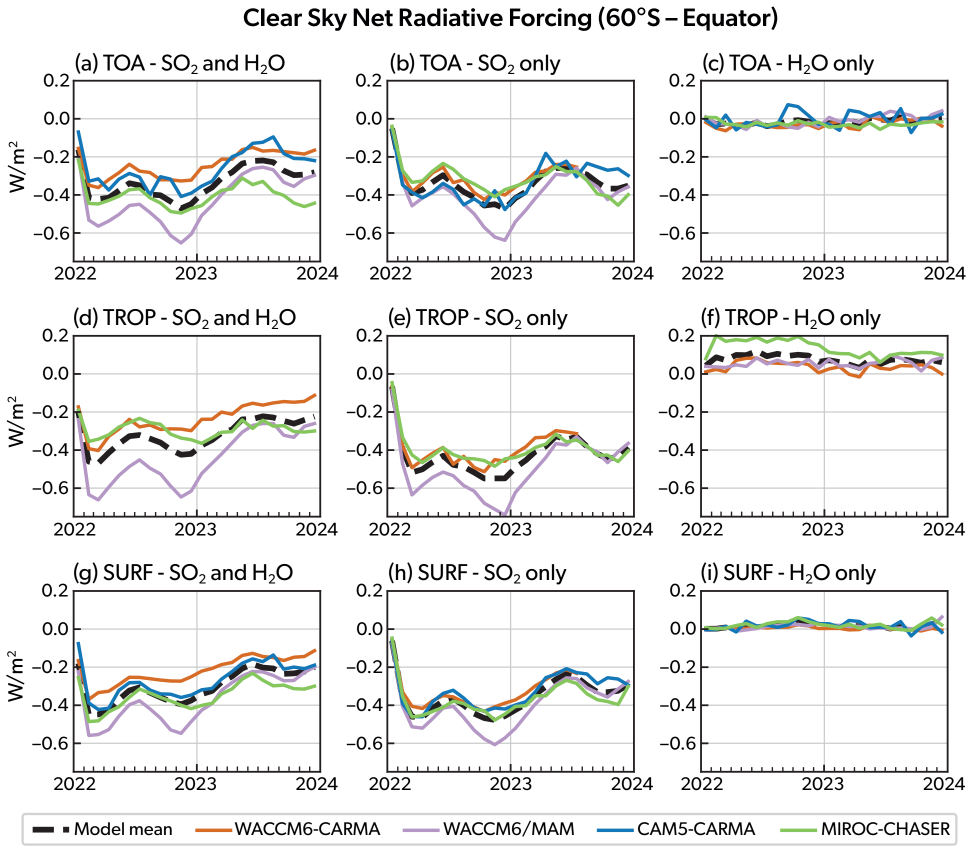

Figure 7.7: *Near-hemispheric (0–60°S) average WV+SA (a, d, g), SA (b, e, h), and WV (c, f, i) clear-sky net IRFs (W m^{-2}) calculated in runs with nudged meteorology for different models, as indicated in the legend, at: (a–c) TOA, (d–f) TROP, and (g–i) SURF. (Adapted from Quaglia et al., 2025.)*

Table 7.2: *Ensemble mean $\overline{\Delta SAT}$ (K) from the WACCM6MAM-co ensemble.*

AREA	6 MONTHS	1 YEAR	2 YEARS	5 YEARS	10 YEARS
LAND	−0.0850	−0.0240	−0.0836	−0.0274	−0.0173
OCEAN	0.0021	−0.0005	−0.0009	0.0038	0.0038
GLOBAL	−0.0295	−0.0086	−0.0303	−0.0074	−0.0004

7.4.2 WV-dominated climate response (2024-2030)

It is expected that the Hunga WV has a residence time of 4–7 years, longer than SAs (Fleming et al., 2024; Schoeberl et al., 2025). However, despite its prolonged presence in the stratosphere, WV's ability to impact surface temperature and climate depends on its altitude and latitudinal distribution (Solomon et al., 2010). Like the transient climate effects of SA, Hunga's WV impact on middle and lower stratosphere temperature and ozone concentration is limited to 2–3 years. As WV ascends into the upper stratosphere and mesosphere, its direct influence on the dynamics and chemistry of the middle and lower stratosphere diminishes. Figure 7.9 presents the ensemble mean zonally averaged temperature responses (Hunga − control) at the surface and in the stratosphere at the 20 hPa and 50 hPa pressure levels, derived from the 30-member WACCM6MAM-fs and WACCM6MAM-co ensembles. In experiments with prescribed SST, Δ*SAT* is negligible within the 60°S–60°N latitude band; however, in coupled ocean-atmosphere simulations, equatorial temperatures exhibit periodic fluctuations with an amplitude of approximately 0.3 K due to ENSO variability. These ensemble-mean equatorial Δ*SAT* perturbations remain detectable even four years post-eruption (Bednarz et al., 2025).

The La Niña could be affected by negative SA RF, and by the northward shift of the intertropical convergence zone (ITCZ) forced by the SA's cooling of the SH (Pausata et al., 2015; Predybaylo et al., 2017). The strengthening of El Niño in 2025–2026 may be

Table 7.3: *Ensemble mean $\overline{\Delta SAT}$ (K) from the WACCN6MAM-fs ensemble.*

AREA	6 MONTHS	1 YEAR	2 YEARS	5 YEARS	10 YEARS
LAND	−0.0052	0.0055	−0.0086	−0.0265	−0.0235
OCEAN	0.0148	0.0026	−0.0008	−0.0007	−0.0020
GLOBAL	0.0072	0.0034	−0.0038	−0.0102	−0.0099

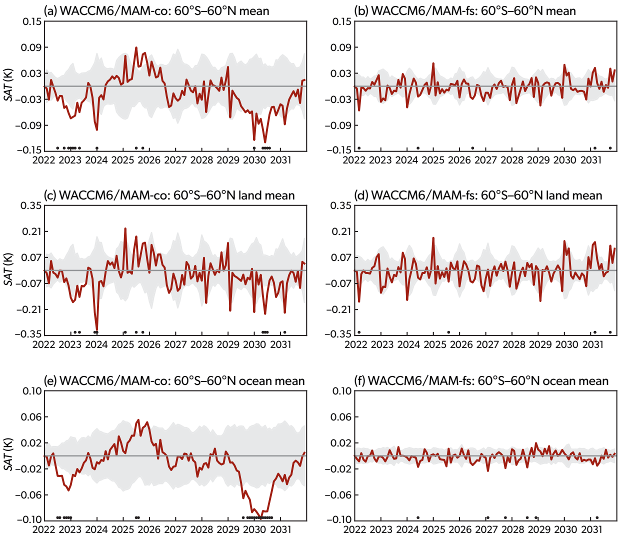

Figure 7.8: *Near-global (60°S-60°N) averaged ensemble mean surface air temperature SAT (K) change (Hunga - control) from the WACCM6MAM-co (left column) and prescribed SST WACCM6MAM-fs (right column) ensembles. Red solid lines show the 30-member ensemble mean. Gray shading belts are ± 2 SAT standard deviations from the control run. (a, b) ΔSAT_G (global), (c, d) ΔSAT_L (land), and (e, f) ΔSAT_O (ocean). Dots at the bottom of the panels indicate the time periods when the SAT perturbation exceeds 2 standard deviations.*

in response to a stronger La Niña in 2022–2023. The enhancement of the ENSO cycle amplitude might potentially affect tropospheric temperature and circulation, as well as cause perturbations in the stratosphere (Simpson et al., 2011; Walsh et al., 2022). However, the perturbations from Hunga are too weak to produce a significant global climate response, and further analysis is required to determine whether the simulated ENSO changes can be attributed to the eruption's impact.

In contrast to the troposphere, the stratosphere exhibits lasting forced temperature signals corresponding to Hunga's water vapour in the upper and lower stratosphere, as well as ozone perturbations in polar regions in both hemispheres (see Figure 7.9 and Chapters 4 and 5). Notably, the stratospheric temperature responses in the coupled-ocean and prescribed SST ensembles were nearly identical in the low and SH midlatitudes but differed in the polar stratosphere. Polar stratospheric cooling may be linked to dynamics (strengthening of the polar vortex) and/or Hunga-induced ozone depletion (see Chapter 5), which could delay (at least in the model) the spring break-up of the polar vortices.

7.4.3 Indirect atmospheric effects

Although Hunga's direct radiative impact on the tropospheric climate is limited, climate feedbacks driven by stratospheric WV perturbations may influence tropospheric conditions. Among the most significant feedback mechanisms are the chemical and dynamical effects of elevated stratospheric WV on ozone concentrations (Fleming et al., 2024; Schoeberl et al., 2024; Evan et al., 2023; Lu et al., 2023; Zhang et al., 2024; Wang et al., 2023; Wilmouth et al., 2023), as well as the stratospheric cooling resulting from WV's radiative effects (Coy et al., 2022; Schoeberl et al., 2022; Kuchar et al., 2025; Bednarz et al., 2025; Niemeier et al., 2023).

Changes in equatorial stratospheric temperatures and polar ozone concentrations modify the meridional temperature gradient between the equator and the poles, thereby influencing stratospheric circulation by strengthening or weakening the polar vortices. These changes involve wave–mean flow interactions and can propagate downward, affecting the troposphere through stratosphere–troposphere dynamical coupling. This coupling can alter the strength and position of the subtropical jet (Thompson and Wallace, 1998; Thompson and Wallace, 2000; Baldwin et al., 2001; Stenchikov et al., 2002; Kuchar et al., 2025; Bednarz et al., 2025). Such interactions may lead to modifications of the Northern Hemisphere (NH) and Southern Hemisphere (SH) annular modes (NAM and SAM), potentially enhancing or weakening them, which in turn influences winter climate in extratropical regions (Ramaswamy, 2006; Shindell et al., 2003; Shindell et al., 2004; Stenchikov et al., 2002; Stenchikov et al., 2004; Stenchikov et al., 2006; Perlwitz and Graf, 2001; Kodera, 1994; Graf et al., 1994).

Hunga's water vapour radiative forcing drives strato-

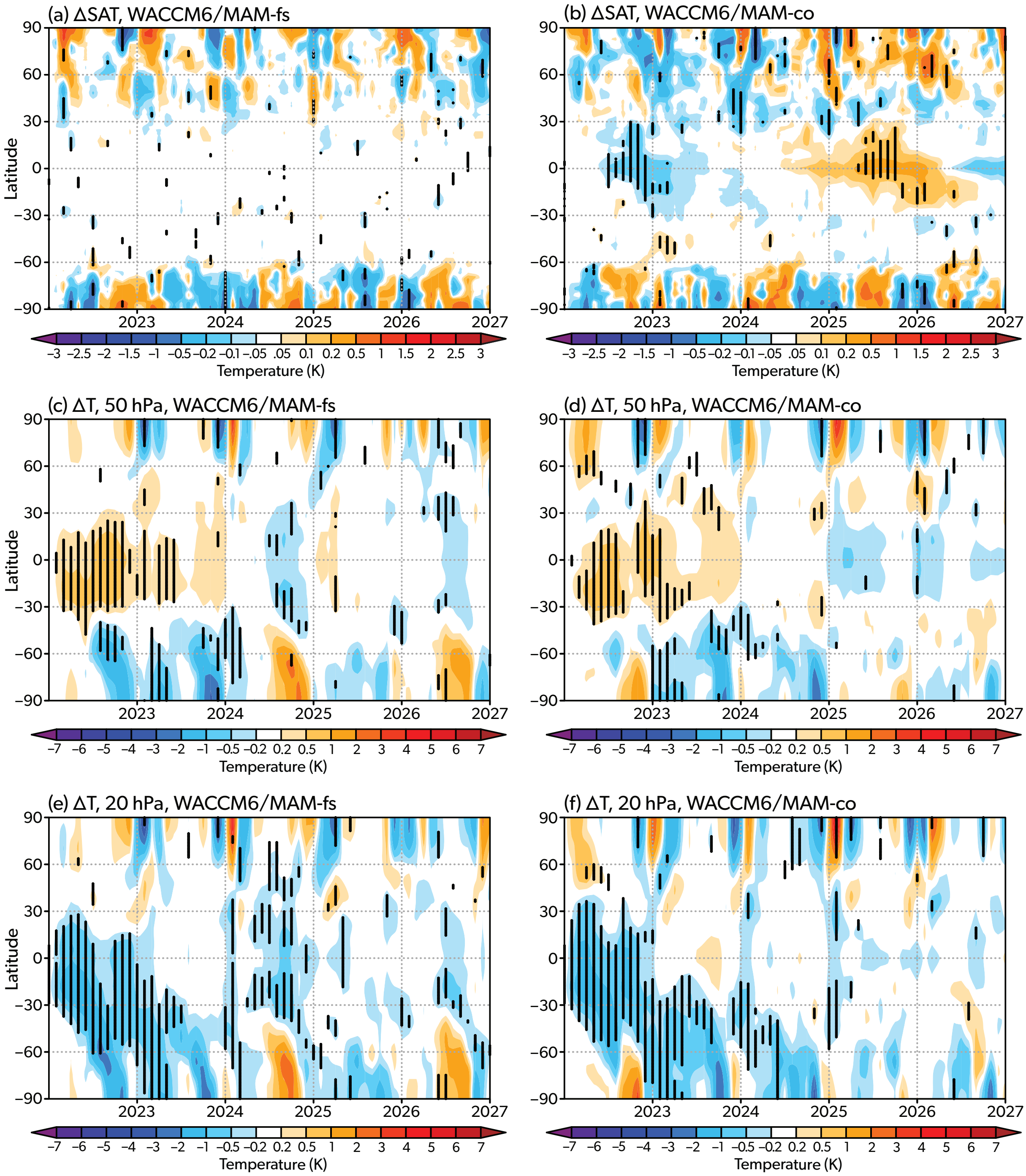

***Figure 7.9:** Zonally averaged ensemble mean perturbations (Hunga - control): (a, b) surface air temperature ΔSAT (K) from WACCM6MAM ensembles with prescribed SSTs (WACCM6MAM-fs) and coupled ocean (WACCM6MAM-co); (c, d) stratospheric temperature (K) at 50 hPa from WACCM6MAM-fs and WACCM6MAM-co; (e, f) stratospheric temperature (K) at 20 hPa from WACCM6MAM-fs and WACCM6MAM-co. Stippling indicates regions where the ensemble mean perturbation exceeds two standard deviations of the corresponding control ensemble mean. (Adapted from Bednarz et al., 2025.)*

spheric temperature perturbations in the middle and upper stratosphere for at least two years, as shown in Figures 7.9c–f and discussed in Chapter 4. In simulations that include both SO_2 and WV emissions, high-latitude ozone perturbations persist for 3–4 years (see Figure 7.10 and Chapters 3 and 4 for further details). As illustrated in Figures 7.9c–f, equatorial temperature anomalies exhibit opposite signs in the lower stratosphere (around 50 hPa) and upper stratosphere (around 20 hPa). This pattern indicates that Hunga's stratospheric temperature perturbations generate positive wind shear in the LS, reinforcing the Southern Hemisphere polar vortex, while inducing negative wind shear in the US, contributing to its weakening. As a result, the Hunga-induced temperature anomalies exert opposing influences on stratospheric circulation in the LS and US, complicating the interpretation of their net effect.

Polar ozone depletion can influence polar temperatures and strengthen the polar vortices, thereby favouring the positive phases of the SAM and NAM (Stenchikov et al., 2002; Waugh and Polvani, 2010; Dennison et al., 2015; Ivy et al., 2017). In the Southern Hemisphere, ozone depletion during the austral springs of 2024 and 2025 is linked to a stronger polar vortex and a delayed final warming. For instance, in the WACCM6MAM-fs and WACCM6MAM-co ensembles, the ozone loss observed during the 2023/2024 austral spring (Figures 7.10a, b) enhances the SH polar vortex, as reflected by stronger zonal winds at 50 hPa near 60°S (Figures 7.10c, d), delays the final warming, and produces a sea-level pressure anomaly consistent with a positive SAM phase (Figures 7.10e, f). Ozone depletion is more pronounced in the WACCM6MAM-fs ensemble compared to WACCM6MAM-co, resulting in larger anomalies in both the 50 hPa zonal wind and sea-level pressure response.

After 2025, Hunga-driven polar ozone perturbations are no longer robust. It is important to emphasise that both polar stratospheric responses and stratosphere–troposphere dynamical coupling are sensitive to model configurations and experimental setups. For example, in the WACCM6MAM-fs and WACCM6MAM-co ensembles (Figures 7.9c, d and 7.10c, d), the ensemble-mean perturbations of the SH and NH polar vortices differ between the ensembles. This inconsistency arises because the forced responses to the Hunga eruption are masked by substantial internal variability in the high-latitude climate.

In contrast to ozone variations in the middle stratosphere, which are more prominent at high southern and northern latitudes (Figures 7.10a, c), ozone perturbations in the upper stratosphere and lower mesosphere are observed primarily in the low and midlatitudes starting in 2024 (see Chapter 5). However, these perturbations lead to only minor changes in the total ozone column, as ozone concentrations at these altitudes are inherently low.

7.4.4 Uncertainties in climate response

To assess the intrinsic uncertainties in model simulations of the long-term SAT response to the 2022 Hunga eruption, we compare the responses from different models participating in HTHH-MOC. The global monthly ensemble mean ΔSAT exhibits significant temporal variability. Among the models, the WACCM6MAM-co ensembles and MIROC-CHASER-fs with prescribed SST demonstrate the most significant variability. It is expected that the coupled model exhibits larger year-to-year variability than the model with prescribed SST. For example, the variance of WACCM6MAM-co's ΔSAT is largest among the presented HTHH-MOC ensembles. However, the MIROC-CHASER-fs (not shown) has larger variance than WACCM6MAM-fs, almost matching the WACCM6MAM-co variability. This indicates that MIROC-CHASER-fs might have larger land temperature variability than WACCM6MAM-fs and WACCM6-MAM-co, even though its SAOD perturbation (see Figure 7.1) is smaller than in the WACCM6MAM-co and WACCM6MAM-fs ensembles.

An integrated average $\overline{\Delta SAT}$ introduced in Eq. 7.4 is more stable than the instantaneous ΔSAT, allowing a more reliable conclusion (see Table 7.4). All models show a negative $\overline{\Delta SAT}$ two years following the eruption, reflecting the integrated effect of negative SA forcing (cooling). The decade-average $\overline{\Delta SAT}$ is also negative across all models. However, their absolute values vary by an order of magnitude.

7.5 Discussion and conclusions

Chapter 7 explores the direct and indirect radiative effects of stratospheric WV and SA from the Hunga eruption and their potential climate impacts. The shallow-underwater eruption of the Hunga volcano was distinctive due to the significant amount of injected WV that is expected to persist in the stratosphere for 4–7 years. Unlike the plumes from the 1991 Pinatubo and 2019 Raikoke eruptions, the Hunga plume was initially injected at altitudes of 30–40 km, with overshoots reaching up to 58 km. It then gradually descended to around 27 km over the follow-

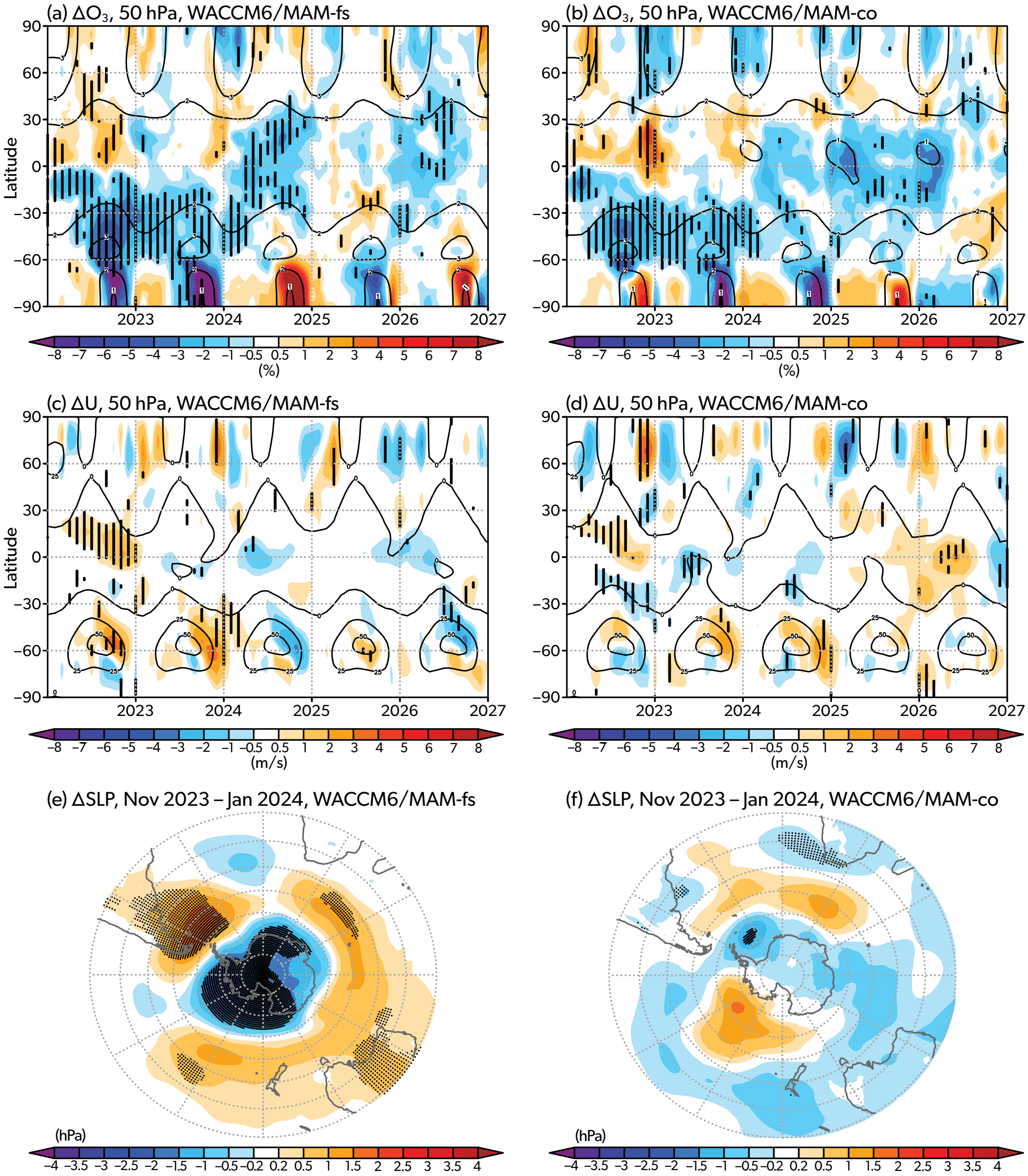

Figure 7.10: *Simulated ensemble-mean zonal-mean ozone changes (%) (Hunga – control) from (a) WACCM6MAM-fs and (b) WACCM6MAM-co. Ensemble-mean zonal-mean zonal wind changes (m s^{-1}) at 50 hPa from (c) WACCM6MAM-fs and (d) WACCM6MAM-co. Mean sea-level pressure changes (hPa) for November 2023–January 2024 (Hunga – control) from (e) WACCM6MAM-fs and (f) WACCM6MAM-co. Hatching indicates regions where the signal exceeds two standard deviations of the ensemble mean. (Adapted from Bednarz et al., 2025.)*

Table 7.4: *Ensemble means $\overline{\Delta SAT}$ (K) from different ensemble simulations.*

Model	6 MONTHS	1 YEAR	2 YEARS	5 YEARS	10 YEARS
WACCM6-MAM-co	−0.0295	−0.0086	−0.0303	−0.0074	−0.0004
WACCM6-MAM-fs	0.0072	0.0034	−0.0038	−0.0102	−0.0099
MIROC-CHASER-fs	−0.0324	−0.0045	−0.0085	−0.0055	−0.0060
GEOSCCM-fs	0.0043	−0.0041	−0.0114	0.0016	−0.0016

ing weeks, staying well above the tropopause (see Chapter 3). The injection height allowed the volcanic plume to initially persist within the high and middle stratosphere, which increased the SAOD per unit mass of emitted SO_2 compared to previous stratospheric penetrating volcanic eruptions (Stenchikov et al., 2025).

In the first two years following the Hunga eruption, the tropospheric cooling caused by stratospheric SAs outweighed the warming due to WV, possibly causing weak, undetectable surface cooling. The radiative impact of stratospheric WV on the tropospheric climate decreases rapidly with the altitude of the WV perturbation (Solomon et al., 2010; Riese et al., 2012; Dessler et al., 2013; Banerjee et al., 2019; Nowack et al., 2023). Since the Hunga eruption injected WV into the middle and upper stratosphere, its overall climate impact is relatively weak despite the substantial increase in stratospheric WV.

The overall (SA + WV) long-term direct radiative effect of Hunga's WV appears to be insignificant; that said, the Hunga eruption presents a unique opportunity to address broader questions regarding climate variability and stratospheric WV feedbacks in global warming (Forster and Shine, 2002; Solomon et al., 2010; Dessler et al., 2013; Charlesworth et al., 2023; Banerjee et al., 2019; Nowack et al., 2023). While WV leads to noticeable radiative cooling in the stratosphere, its IRF and ERF at TOA are minimal. As a result, the direct RF from WV is insufficient to trigger slow climate feedback mechanisms linked to ocean heat content (Sellitto et al., 2022; Stenchikov et al., 2025), and its radiative influence will diminish as the WV forcing decreases.

The main findings of this Chapter are as follows:

- Hunga's water vapour initially produced strong localised radiative cooling in the stratosphere, in contrast to the radiative heating typically caused by volcanic ash in the lower stratosphere following major explosive eruptions (e.g., the 1991 Pinatubo eruption).
- Accurate simulation of the Hunga cloud's initial evolution is critical, as WV phase transitions and the early dispersion of WV, SO_2, and SA strongly depend on injection altitude – a key factor in shaping its long-term behaviour. However, both observations and the HTHH-MOC models only partially capture the descent trajectory of the fresh Hunga cloud.
- Calculating IRF in HTHH-MOC models based on radiative flux differences between perturbed and control runs with nudged meteorology presents challenges in interpreting RF contributions from SA and WV. This approach introduces contamination from ozone and PSC effects, making it difficult to isolate the individual RFs of WV and SA. Integrating a double-call capability into the standard climate model configuration would help mitigate this issue, allowing for more precise attribution of radiative forcing components.
- Estimating SA radiative forcing using SO_2-only simulations may be unreliable, as the absence of WV-induced cooling prevents plume descent and leads to a markedly different evolution compared to simulations with concurrent WV and SO_2 emissions. However, in the WACCM6MAM experiments, this approach remained effective due to the relatively low injection height (~30 km), placing the plume near its level of neutral buoyancy.
- Comparison of stratospheric aerosol simulations with observations indicates that the Hunga volcano injected between 0.65 and 1.0 Tg of SO_2, with initial observational estimates falling at the lower end of this range.
- During the first two years (2022-2023), the radiative effects of WV and SAs counteract each other: WV cools the stratosphere and warms the troposphere, while SAs warm the stratosphere and cool the troposphere. This has not been observed in previous volcanic eruptions. Sulfate aerosol RF dominates in 2022-2023, while WV RF becomes dominant (but tiny) in 2024-2031. On average in 2022-2023, a

net global SA+WV IRF and ERF are about −0.4 W/m^2 at all atmospheric levels.

- WV IRF at TOA is negative, but ERF is positive, proving that Hunga's WV has a net (but very minor) warming effect on the planet. The WV RF is small at TOA and tropopause, and negligible at SURF, suggesting that the Hunga WV direct radiative impacts on climate are insignificant.
- Hunga's RF causes global 0.3-0.4 K cooling in the middle and upper stratosphere, but the domain average maximum $\overline{\Delta SAT}$ is weaker than −0.05 K, remaining within the bounds of natural variability.
- Climate model simulations show that Hunga may have had a very slight influence on the timing of ENSO and produced slight shifts in the subtropical jet. These changes would be overwhelmed by natural variability. The overall long-term SAT perturbations caused by the Hunga eruption are hardly detectable in the model simulations.

References

Abdelkader, M., G. Stenchikov, A. Pozzer, H. Tost and J. Lelieveld (2023). 'The effect of ash, water vapor, and heterogeneous chemistry on the evolution of a Pinatubo-size volcanic cloud'. *Atmos. Chem. Phys.*, 23, pp. 471–500. DOI: `10.5194/acp-23-471-2023`.

Andersson, S. M., B. G. Martinsson, J. P. Vernier, J. Friberg, C. A. Brenninkmeijer, M. Hermann and A. Zahn (2015). 'Significant radiative impact of volcanic aerosol in the lowermost Stratosphere'. *Nat. Commun.*, 6, 7692. DOI: `10.1038/ncomms8692`.

Andrews, T., C. J. Smith, G. Myhre, P. M. Forster, R. Chadwick and D. Ackerley (2021). 'Effective Radiative Forcing in a GCM With Fixed Surface Temperatures'. *J. Geophys. Res.*, 126, e2020JD033880. DOI: `10.1029/2020jd033880`.

Appenzeller, C., J. R. Holton and K. H. Rosenlof (1996). 'Seasonal variation of mass transport across the tropopause'. *J. Geophys. Res.*, 101, pp. 15071–15078. DOI: `10.1029/96JD00821`.

Baldwin, M. P., L. J. Gray, T. J. Dunkerton, K. Hamilton, P. H. Haynes, W. J. Randel, J. Holton, M. J. Alexander, I. Hirota and T. Horinouchi (2001). 'The quasi-biennial oscillation'. *Rev. Geophys.*, 39, pp. 179–229. DOI: `10.1029/1999rg000073`.

Banerjee, A., G. Chiodo, M. Previdi, M. Ponater, A. J. Conley and L. M. Polvani (2019). 'Stratospheric water vapor: an important climate feedback'. *Clim. Dynam.*, 53, pp. 1697–1710. DOI: `10.1007/s00382-019-04721-4`.

Baran, A. J. and J. S. Foot (1994). 'New application of the operational sounder HIRS in determining a climatology of sulphuric acid aerosol from the Pinatubo eruption'. *J. Geophys. Res.*, 99, pp. 25673–25679. DOI: `10.1029/94JD02044`.

Barnes, J. E. and D. J. Hofmann (1997). 'Lidar measurements of stratospheric aerosol over Mauna Loa Observatory'. *Geophys. Res. Lett.*, 24, pp. 1923–1926. DOI: `10.1029/97GL01943`.

Baron, A., P. Chazette, S. Khaykin, G. Payen, N. Marquestaut, N. Bègue and V. Duflot (2023). 'Early Evolution of the Stratospheric Aerosol Plume Following the 2022 Hunga Tonga-Hunga Ha'apai Eruption: Lidar Observations From Reunion (21°S, 55°E)'. *Geophys. Res. Lett.*, 50, e2022GL101751. DOI: `10.1029/2022gl101751`.

Bednarz, E. M., A. H. Butler, X. Wang, Z. Zhuo, W. Yu, G. Stenchikov, M. Toohey and Y. Zhu (2025). 'Indirect climate impacts of the Hunga eruption'. *EGUsphere [preprint]*, DOI: `10.5194/egusphere-2025-1970`.

Bluth, G. J., W. I. Rose, I. E. Sprod and A. J. Krueger (1997). 'Stratospheric Loading of Sulfur From Explosive Volcanic Eruptions'. *J. Geol.*, 105, pp. 671–684. DOI: `10.1086/515972`.

Bluth, G. J. S., S. D. Doiron, C. C. Schnetzler, A. J. Krueger and L. S. Walter (1992). 'Global tracking of the SO_2 clouds from the June, 1991 Mount Pinatubo eruptions'. *Geophys. Res. Lett.*, 19, pp. 151–154. DOI: `10.1029/91GL02792`.

Bourassa, A. E., D. J. Zawada, L. A. Rieger, T. W. Warnock, M. Toohey and D. A. Degenstein (2023). 'Tomographic retrievals of Hunga Tonga-Hunga Ha'apai volcanic aerosol'. *Geophys. Res. Lett.*, 50, e2022GL101978. DOI: `10.1029/2022GL101978`.

Carn, S. A., L. Clarisse and A. J. Prata (2016). 'Multi-decadal satellite measurements of global volcanic degassing'. *J. Volcanol. Geotherm. Res.*, 311, pp. 99–134. DOI: `10.1016/j.jvolgeores.2016.01.002`.

Carn, S. A., N. A. Krotkov, B. L. Fisher and C. Li (2022). 'Out of the blue: volcanic SO_2 emissions during the 2021-2022 Hunga Tonga-Hunga Ha'apai eruptions'. *Front. Earth Sci.*, 13. DOI: `10.3389/feart.2022.976962`.

Charlesworth, E., F. Plöger, T. Birner, R. Baikhadzhaev, M. Abalos, N. L. Abraham and M. Riese (2023). 'Stratospheric water vapor affecting atmospheric circulation'. *Nat. Commun.*, 14, 3925. DOI: `s41467-023-39559-2`.

Chen, P., M. Xiong, R. Wang, Y. Yao, F. Tang, H. Chen and L. Qiu (2023). 'On the ionospheric disturbances in New Zealand and Australia following the eruption of the Hunga Tonga-Hunga Ha'apai volcano on 15 January 2022'. *Geoph. Monog. Series.*, 21, e2022SW003294. DOI: `10.1029/2022SW003294`.

Chiou, E. W., L. W. Thomason and W. P. Chu (2006). 'Variability of Stratospheric Water Vapor Inferred from SAGE II, HALOE, and Boulder (Colorado) Balloon Measurements'. *J. Climate*, 19, pp. 4121–4133. DOI: `10.1175/JCLI3841.1`.

Coy, L., P. Newman, K. Wargan, G. Partyka, S. Strahan and S. Pawson (2022). 'Stratospheric Circulation Changes Associated with the Hunga Tonga-Hunga Ha'apai Eruption'. *Geophys. Res. Lett.*, 49, e2022GL100982. DOI: `10.1029/2022GL100982`.

Delworth, T. L., A. J. Broccoli, A. Rosati, R. J. Stouffer, V. Balaji, J. A. Beesley, W. F. Cooke, K. W. Dixon, J. Dunne, K. A. Dunne et al. (2006). 'GFDL's CM2 global coupled climate models. Part I: Formulation and simulation characteristics'. *J. Climate*, 19, pp. 643–674. DOI: `10.1175/JCLI3629.1`.

Dennison, F. W., A. J. McDonald and O. Morgenstern (2015). ‘The effect of ozone depletion on the Southern Annular Mode and stratosphere–troposphere coupling’. *J. Geophys. Res.*, 120, pp. 6305–6312. DOI: `10.1002/2014JD023009`.

Deshler, T. (2008). ‘A review of global stratospheric aerosol: Measurements, importance, life cycle and local stratospheric aerosol’. *Atmos. Res.*, 90, pp. 223–232. DOI: `10.1016/j.atmosres.2008.03.016`.

Dessler, A. E., M. R. Schoeberl, T. Wang, S. Davis and K. H. Rosenlof (2013). ‘Stratospheric water vapor feedback’. *Proc. Natl. Acad. Sci.*, 110, pp. 18087–18091. DOI: `10.1073/pnas.1310344110`.

Duchamp, C., F. Wrana, B. Legras, P. Sellitto, R. Belhadji and C. von Savigny (2023). ‘Observation of the aerosol plume from the 2022 Hunga Tonga–Hunga Ha’apai eruption with SAGE III/ISS’. *Geophys. Res. Lett.*, 50, e2023GL105076. DOI: `10.1029/2023GL105076`.

Dutton, E. and J. DeLuisi (1983). ‘Spectral extinction of direct solar radiation by the El Chichón cloud during December 1982’. *Geophys. Res. Lett.*, 10, pp. 1013–1016. DOI: `10.1029/GL010i011p01013`.

Dutton, E. G. and J. R. Christy (1992). ‘Solar radiative forcing at selected locations and evidence for global lower tropospheric cooling following the eruptions of El Chichón and Pinatubo’. *Geophys. Res. Lett.*, 19, pp. 2313–2316. DOI: `10.1029/92GL02495`.

Dutton, E. G., P. Reddy, S. Ryan and J. J. DeLuisi (1994). ‘Features and effects of aerosol optical depth observed at Mauna Loa, Hawaii: 1982–1992’. *J. Geophys. Res.*, 99, pp. 8295–8306. DOI: `10.1029/93JD03520`.

Evan, S., J. Brioude, K. H. Rosenlof, R.-S. Gao, R. W. Portmann, Y. Zhu, R. Volkamer, C. F. Lee, J.-M. Metzger, K. Lamy et al. (2023). ‘Rapid ozone depletion after humidification of the stratosphere by the Hunga Tonga eruption’. *Science*, 382, eadg2551. DOI: `10.1126/science.adg2551`.

Fahey, D. W., K. K. Kelly, S. R. Kawa, A. F. Tuck, M. Loewenstein, K. R. Chan and L. E. Heidt (1990). ‘Observations of denitrification and dehydration in the winter polar stratospheres’. *Nature*, 344, pp. 321–324. DOI: `10.1038/344321a0`.

Fels, S. B., J. D. Mahlman, M. D. Schwarzkopf and R. W. Sinclair (1980). ‘Stratospheric sensitivity to perturbations in ozone and carbon dioxide: Radiative and dynamical response’. *J. Atmos. Sci.*, 37, pp. 2265–2297. DOI: `10.1175/1520-0469(1980)037%3C2265:SSTPIO%3E2.0.CO;2`.

Fleming, E. L., P. A. Newman, Q. Liang and L. D. Oman (2024). ‘Stratospheric Temperature and Ozone Impacts of the Hunga Tonga-Hunga Ha’apai Water Vapor Injection’. *J. Geophys. Res.*, 129, e2023JD039298. DOI: `10.1029/2023jd039298`.

Forster, P. M., V. I. Fomichev, E. Rozanov, C. Cagnazzo, A. I. Jonsson, U. Langematz and K. Shibata (2011). ‘Evaluation of radiation scheme performance within chemistry climate models’. *J. Geophys. Res.*, 116, D10302. DOI: `10.1029/2010JD015361`.

Forster, P. M., T. Richardson, A. C. Maycock, C. J. Smith, B. H. Samset, G. Myhre and M. Schulz (2016). ‘Recommendations for diagnosing effective radiative forcing from climate models for CMIP6’. *J. Geophys. Res.*, 121, pp. 12460–12475. DOI: `10.1002/2016JD025320`.

Forster, P. M. D. and K. P. Shine (1999). ‘Stratospheric water vapour changes as a possible contributor to observed stratospheric cooling’. *Geophys. Res. Lett.*, 26, pp. 3309–3312. DOI: `10.1029/1999GL010487`.

Forster, P. M. D. F. and K. P. Shine (2002). ‘Assessing the climate impact of trends in stratospheric water vapor’. *Geophys. Res. Lett.*, 29. DOI: `10.1029/2001GL013909`.

Fueglistaler, S., Y. S. Liu, T. J. Flannaghan, P. H. Haynes, D. P. Dee, W. J. Read and P. F. Bernath (2013). ‘The relation between atmospheric humidity and temperature trends for stratospheric water’. *J. Geophys. Res.*, 118, pp. 1052–1074. DOI: `10.1002/jgrd.50157`.

Graf, H., J. Perlwitz and I. Kirchner (1994). ‘Northern Hemisphere tropospheric mid-latitude circulation after violent volcanic eruptions’. *Contrib. Atmos. Phys. (also Beitr. Phys. Atmosph.)*, 67, pp. 3–13.

Guo, S., G. J. Bluth, W. I. Rose, I. M. Watson and A. J. Prata (2004a). ‘Re-evaluation of SO_2 release of the 15 June 1991 Pinatubo eruption using ultraviolet and infrared satellite sensors’. *Geochem. Geophys. Geosyst.*, 5, Q04001. DOI: `10.1029/2003GC000654`.

Guo, S., W. I. Rose, G. J. Bluth and I. M. Watson (2004b). ‘Particles in the great Pinatubo volcanic cloud of June 1991: The role of ice’. *Geochem. Geophys. Geosyst.*, 5, Q05003. DOI: `10.1029/2003GC000655`.

Gupta, A. K., T. Mittal, K. E. Fauria, R. Bennartz and J. F. Kok (2025). ‘The January 2022 Hunga eruption cooled the Southern Hemisphere in 2022 and 2023’. *Commun. Earth Environ.*, 6, 240. DOI: `10.1038/s43247-025-02181-9`.

Hamill, P., E. J. Jensen, P. B. Russell and J. J. Bauman (1997). ‘The life cycle of stratospheric aerosol particles’. *Bull. Am. Meteorol. Soc.*, 7, pp. 1395–1410.

DOI: `10.1175/1520-0477(1997)078<1395:tlcosa>2.0.co;2`.

Hansen, J. (2002). 'Climate forcing in Goddard Institute for Space Studies SI2000 simulations'. *J. Geophys. Res.*, 107, 4347. DOI: `10.1029/2001jd001143`.

Hansen, J., M. Sato, R. Ruedy, L. Nazarenko, A. Lacis, G. Schmidt, G. Russell, I. Aleinov, M. Bauer and S. Bauer (2005). 'Efficacy of climate forcings'. *J. Geophys. Res.*, 110, D18104. DOI: `10.1029/2005jd005776`.

He, R. and Y. Huang (2025). 'Muted radiative feedback of stratospheric water vapor found in a multimodel assessment'. *J. Geophys. Res.*, 130, e2025JD043676. DOI: `10.1029/2025jd043676`.

Holton, J. R., P. H. Haynes, M. E. McIntyre, A. R. Douglass, R. B. Rood and L. Pfister (1995). 'Stratosphere-troposphere exchange'. *Rev. Geophys.*, 33, pp. 403–439. DOI: `10.1029/95rg02097`.

Höpfner, M., C. D. Boone, B. Funke, N. Glatthor, U. Grabowski, A. Günther, S. Kellmann, M. Kiefer, A. Linden, S. Lossow et al. (2015). 'Sulfur dioxide (SO_2) from MIPAS in the upper troposphere and lower stratosphere 2002–2012'. *Atmos. Chem. Phys.*, 15, pp. 7017–7037. DOI: `10.5194/acp-15-7017-2015`.

Huang, Y., Y. Wang and H. Huang (2020). 'Stratospheric water vapor feedback disclosed by a locking experiment'. *Geophys. Res. Lett.*, 47, e2020GL087987. DOI: `10.1029/2020gl087987`.

Ivy, D. J., S. Solomon, N. Calvo and D. W. Thompson (2017). 'Observed connections of Arctic stratospheric ozone extremes to Northern Hemisphere surface climate'. *Environ. Res. Lett.*, 12, 024004. DOI: `10.1088/1748-9326/aa57a4`.

Jenkins, S., C. Smith, M. Allen and R. Grainger (2023). 'Tonga eruption increases chance of temporary surface temperature anomaly above 1.5° C'. *Nat. Clim. Change*, 13, pp. 127–129. DOI: `10.1038/s41558-022-01568-2`.

Johnson, J., G. Taha, R. Loughman, T. Zhu and M. DeLand (2025). *README Document for the Suomi-NPP OMPS LP L2 AER Daily Product, Collection 2.5, Version 2.5.* Tech. rep. `https://disc.gsfc.nasa.gov/`, Last access: 14 August 2025. Greenbelt, MD, USA: NASA GES DISC.

Joshi, M. M. and G. S. Jones (2009). 'The climatic effects of the direct injection of water vapour into the stratosphere by large volcanic eruptions'. *Atmos. Chem. Phys.*, 9, pp. 6109–6118. DOI: `10.5194/acp-9-6109-2009`.

Joshi, M. M. and K. P. Shine (2003). 'A GCM Study of Volcanic Eruptions as a Cause of Increased Stratospheric Water Vapor'. *J. Climate*, 16, pp. 3525–3534. DOI: `10.1175/1520-0442(2003)016<3525:AGSOVE>2.0.CO;2`.

Jucker, M., C. Lucas and D. Dutta (2024). 'Long-term climate impacts of large stratospheric water vapor perturbations'. *J. Climate*, 37, pp. 4507–4521. DOI: `10.1175/JCLI-D-23-0437.1`.

Kelly, K. K., A. F. Tuck, D. M. Murphy, M. H. Proffitt, D. W. Fahey, R. L. Jones, D. S. McKenna, M. Loewenstein, J. R. Podolske, S. E. Strahan et al. (1989). 'Dehydration in the lower Antarctic stratosphere during late winter and early spring, 1987'. *J. Geophys. Res.*, 94, pp. 11317–11357. DOI: `10.1029/jd094id09p11317`.

Khaykin, S., A. Podglajen, F. Ploeger, J.-U. Grooß, F. Tence, S. Bekki, K. Khlopenkov, K. Bedka, L. Rieger, A. Baron et al. (2022). 'Global perturbation of stratospheric water and aerosol burden by Hunga eruption'. *Commun. Earth Environ.*, 3, 316. DOI: `10.1038/s43247-022-00652-x`.

Kloss, C., P. Sellitto, J.-B. Renard, A. Baron, N. Bègue, B. Legras, G. Berthet, E. Briaud, E. Carboni, C. Duchamp et al. (2022). 'Aerosol characterization of the stratospheric plume from the volcanic eruption at Hunga Tonga 15 January 2022'. *Geophys. Res. Lett.*, 49, e2022GL099394. DOI: `10.1029/2022GL099394`.

Kodera, K. (1994). 'Influence of volcanic eruptions on the troposphere through stratospheric dynamical processes in the Northern Hemisphere winter'. *J. Geophys. Res.*, 99, pp. 1273–1282. DOI: `10.1029/93JD02731`.

Kovilakam, M., L. W. Thomason, N. Ernest, L. Rieger, A. Bourassa and L. Millán (2020). 'The Global Space-based Stratospheric Aerosol Climatology (version 2.0): 1979–2018'. *Earth Syst. Sci. Data*, 12, pp. 2607–2634. DOI: `10.5194/essd-12-2607-2020`.

Kremser, S., L. W. Thomason, M. Von Hobe, M. Hermann, T. Deshler, C. Timmreck, M. Toohey, A. Stenke, J. P. Schwarz, R. Weigel et al. (2016). 'Stratospheric aerosol-Observations, processes, and impact on climate: Stratospheric Aerosol'. *Rev. Geophys.*, 54, pp. 278–335. DOI: `10.1002/2015RG000511`.

Kroll, C. A., S. Dacie, A. Azoulay, H. Schmidt and C. Timmreck (2021). 'The impact of volcanic eruptions of different magnitude on stratospheric water vapor in the tropics'. *Atmos. Chem. Phys.*, 21, pp. 6565–6591. DOI: `10.5194/acp-21-6565-2021`.

Kroll, C. A. and A. Schmidt (2024). 'Indirect stratospheric moisture increase after a Pinatubo-magnitude eruption can be comparable to direct increase after 2022 Hunga'. *Commun. Earth Environ.*, 5, 497. DOI: `10.1038/s43247-024-01651-w`.

Kuchar, A., T. Sukhodolov, G. Chiodo, A. Jörimann, J. Kult-Herdin, E. Rozanov and H. H. Rieder (2025). 'Modulation of the northern polar vortex by the Hunga Tonga–Hunga Ha'apai eruption and the associated surface response'. *Atmos. Chem. Phys.*, 25, pp. 3623–3634. DOI: `10.5194/acp-25-3623-2025`.

Lacis, A., J. Hansen and M. Sato (1992). 'Climate forcing by stratospheric aerosols'. *Geophys. Res. Lett.*, 19, pp. 1607–1610. DOI: `10.1029/92gl01620`.

Lambert, A., R. G. Grainger, J. J. Remedios, C. D. Rodgers, M. Corney and F. W. Taylor (1993). 'Measurements of the evolution of the Mt. Pinatubo aerosol cloud by ISAMS'. *Geophys. Res. Lett.*, 20, pp. 1287–1290. DOI: `10.1029/93gl00827`.

Larson, E. J. and R. W. Portmann (2016). 'A temporal kernel method to compute effective radiative forcing in CMIP5 transient simulations'. *J. Climate*, 29, pp. 1497–1509. DOI: `10.1175/jcli-d-15-0577.1`.

LeGrande, A., K. Tsigaridis and S. Bauer (2016). 'Role of atmospheric chemistry in the climate impacts of stratospheric volcanic injections'. *Nat. Geosci.*, pp. 652–655. DOI: `10.1038/ngeo2771`.

Legras, B., C. Duchamp, P. Sellitto, A. Podglajen, E. Carboni, R. Siddans, J.-U. Grooß, S. Khaykin and F. Ploeger (2022). 'The evolution and dynamics of the Hunga Tonga–Hunga Ha'apai sulfate aerosol plume in the stratosphere'. *Atmos. Chem. Phys.*, 22, pp. 14957–14970. DOI: `10.5194/acp-22-14957-2022`.

Li, F. and P. Newman (2020). 'Stratospheric water vapor feedback and its climate impacts in the coupled atmosphere–ocean Goddard Earth Observing System Chemistry-Climate Model'. *Clim. Dynam.*, 55, pp. 1585–1595. DOI: `10.1007/s00382-020-05348-6`.

Lu, J., S. Lou, X. Huang, L. Xue, K. Ding, T. Liu, Y. Ma, W. Wang and A. Ding (2023). 'Stratospheric aerosol and ozone responses to the Hunga Tonga-Hunga Ha'apai volcanic eruption'. *Geophys. Res. Lett.*, 50, e2022GL102315. DOI: `10.1029/2022GL102315`.

Marshall, L. R., E. C. Maters, A. Schmidt, C. Timmreck, A. Robock and M. Toohey (2022). 'Volcanic effects on climate: recent advances and future avenues'. *B. Volcanol.*, 84, 54. DOI: `10.1007/s00445-022-01559-3`.

Marshall, L. R., C. J. Smith, P. M. Forster, T. J. Aubry, T. Andrews and A. Schmidt (2020). 'Large Variations in Volcanic Aerosol Forcing Efficiency Due to Eruption Source Parameters and Rapid Adjustments'. *Geophys. Res. Lett.*, 47, e2020GL090241. DOI: `10.1029/2020GL090241`.

Maycock, A. C. and K. P. Shine (2012). 'Stratospheric water vapor and climate: Sensitivity to the representation in radiation codes'. *J. Geophys. Res.*, 117, D13102. DOI: `10.1029/2012JD017484`.

Maycock, A. C., M. M. Joshi, K. P. Shine and A. A. Scaife (2013). 'The Circulation Response to Idealized Changes in Stratospheric Water Vapor'. *J. Climate*, 26, pp. 545–561. DOI: `10.1175/JCLI-D-12-00155.1`.

Millán, L., W. G. Read, M. L. Santee, A. Lambert, G. L. Manney, J. L. Neu, M. C. Pitts, F. Werner, N. J. Livesey and M. J. Schwartz (2024). 'The Evolution of the Hunga Hydration in a Moistening Stratosphere'. *Geophys. Res. Lett.*, 51, e2024GL110841. DOI: `10.1029/2024gl110841`.

Millán, L., M. L. Santee, A. Lambert, N. J. Livesey, F. Werner, M. J. Schwartz, H. C. Pumphrey, G. L. Manney, Y. Wang, H. Su et al. (2022). 'The Hunga Tonga-Hunga Ha'apai Hydration of the Stratosphere'. *Geophys. Res. Lett.*, 49, e2022GL099381. DOI: `10.1029/2022gl099381`.

Mills, M. J., A. Schmidt, R. Easter, S. Solomon, D. E. Kinnison, S. J. Ghan et al. (2016). 'Global volcanic aerosol properties derived from emissions, 1990–2014, using CESM1 (WACCM)'. *J. Geophys. Res.*, 121, pp. 2332–2348. DOI: `10.1002/2015jd024290`.

Minnis, P., E. F. Harrison, L. L. Stowe, G. G. Gibson, F. M. Denn, D. R. Doelling and W. L. J. Smith (1993). 'Radiative climate forcing by the Mt. Pinatubo eruption'. *Science*, 259, pp. 1411–1415. DOI: `10.1126/science.259.5100.1411`.

Muthers, S., F. Arfeuille, C. C. Raible and E. Rozanov (2015). 'The impacts of volcanic aerosol on stratospheric ozone and the Northern Hemisphere polar vortex: separating radiative-dynamical changes from direct effects due to enhanced aerosol heterogeneous chemistry'. *Atmos. Chem. Phys.*, 15, pp. 11461–11476. DOI: `10.5194/acp-15-11461-2015`.

Nedoluha, G. E., R. M. Bevilacqua and K. W. Hoppel (2002). 'POAM III measurements of dehydration in the Antarctic and comparisons with the Arctic'. *J. Geophys. Res.*, 107, 8290. DOI: `10.1029/2001JD001184`.

Nedoluha, G. E., R. M. Gomez, I. Boyd, H. Neal, D. R. Allen and A. Lambert (2024). 'The Spread of the Hunga Tonga H2O Plume in the Middle Atmosphere Over the First Two Years Since Eruption'. *J.*

Geophys. Res., 129, e2024JD040907. DOI: `10.1029/2024jd040907`.

Newhall, C. and S. Self (1982). 'The volcanic explosivity index (VEI) an estimate of explosive magnitude for historical volcanism'. *J. Geophys. Res.*, 87, pp. 1231–1238. DOI: `10.1029/hg002p0143`.

Niemeier, U., C. Timmreck, H.-F. Graf, S. Kinne, S. Rast and S. Self (2009). 'Initial fate of fine ash and sulfur from large volcanic eruptions'. *Atmos. Chem. Phys.*, 9, pp. 9043–9057. DOI: `10.5194/acp-9-9043-2009`.

Niemeier, U., S. Wallis, C. Timmreck, T. van Pham and C. von Savigny (2023). 'How the Hunga Tonga—Hunga Ha'apai Water Vapor Cloud Impacts Its Transport Through the Stratosphere: Dynamical and Radiative Effects'. *Geophys. Res. Lett.*, 50, e2023GL106482. DOI: `10.1029/2023gl106482`.

Nowack, P., P. Ceppi, S. M. Davis, G. Chiodo, W. Ball, M. A. Diallo, B. Hassler, Y. Jia, J. Keeble and M. Joshi (2023). 'Response of stratospheric water vapour to warming constrained by satellite observations'. *Nat. Geosci.*, 16, pp. 577–583. DOI: `10.1038/s41561-023-01183-6`.

Oman, L., A. Robock, G. Stenchikov, T. Thordarson, D. Koch, D. Shindell and C. Gao (2006). 'Modeling the distribution of the volcanic aerosol cloud from the 1783–1784 Laki eruption'. *J. Geophys. Res.*, 111, D12209. DOI: `10.1029/2005jd006899`.

Pausata, F. S., L. Chafik, R. Caballero and D. S. Battisti (2015). 'Impacts of high-latitude volcanic eruptions on ENSO and AMOC'. *Proc. Nat. Acad. Sci.*, 112, pp. 13784–13788. DOI: `10.1073/pnas.1509153112`.

Perlwitz, J. and H.-F. Graf (2001). 'Troposphere-stratosphere dynamic coupling under strong and weak polar vortex conditions'. *Geophys. Res. Lett.*, 28, pp. 271–274. DOI: `10.1029/2000GL012405`.

Predybaylo, E., G. L. Stenchikov, A. T. Wittenberg and F. Zeng (2017). 'Impacts of a Pinatubo-Size Volcanic Eruption on ENSO'. *J. Geophys. Res.*, 122, pp. 925–947. DOI: `10.1002/2016JD025796`.

Pueschel, R. F. (1996). 'Stratospheric Aerosols: Formation, Properties, Effects'. *J. Aerosol Sci.*, 27, pp. 383–402. DOI: `10.1016/0021-8502(95)00557-9`.

Quaglia, I., D. Visioni, E. M. Bednarz, Y. Zhu, G. Stenchikov, V. Aquila, C.-C. Liu, G. W. Mann, Y. Peng, T. Sekiya et al. (2025). 'Multi-model analysis of the radiative impacts of the 2022 Hunga eruption indicates a significant cooling contribution from the volcanic plume'. *EGUsphere [preprint]*, 2025, pp. 1–35. DOI: `10.5194/egusphere-2025-3769`.

Quaglia, I., C. Timmreck, U. Niemeier, D. Visioni, G. Pitari, C. Brodowsky, C. Brühl, S. S. Dhomse, H. Franke, A. Laakso et al. (2023). 'Interactive stratospheric aerosol models' response to different amounts and altitudes of SO_2 injection during the 1991 Pinatubo eruption'. *Atmos. Chem. Phys.*, 23, pp. 921–948. DOI: `10.5194/acp-23-921-2023`.

Ramaswamy, V., W. Collins, J. Haywood, J. Lean, N. Mahowald, G. Myhre and T. Storelvmo (2019). 'Radiative forcing of climate: The historical evolution of the radiative forcing concept, the forcing agents and their quantification, and applications'. *Meteor. Mon.*, 59, pp. 14.1–14.101. DOI: `10.1175/AMSMONOGRAPHS-D-19-0001.1`.

Ramaswamy, V. e. a. (2006). 'Anthropogenic and natural influences in the evolution of lower stratospheric cooling'. *Science*, 311, pp. 1138–1141. DOI: `10.1126/science.1122587`.

Randel, W. J., B. R. Johnston, J. J. Braun, S. Sokolovskiy, H. Vömel, A. Podglajen and B. Legras (2023). 'Stratospheric Water Vapor from the Hunga Tonga–Hunga Ha'apai Volcanic Eruption Deduced from COSMIC-2 Radio Occultation'. *Remote Sens.*, 15, 2167, p. 2167. DOI: `10.3390/rs15082167`.

Randel, W. J., F. Wu, S. J. Oltmans, K. Rosenlof and G. E. Nedoluha (2004). 'Interannual Changes of Stratospheric Water Vapor and Correlations with Tropical Tropopause Temperatures'. *J. Atmos. Res.*, 61, pp. 2133–2148. DOI: `10.1175/1520-0469(2004)061<2133:icoswv>2.0.co;2`.

Read, W. G., L. Froidevaux and J. W. Waters (1993). 'Microwave limb sounder measurement of stratospheric SO_2 from the Mt. Pinatubo Volcano'. *Geophys. Res. Lett.*, 20, pp. 1299–1302. DOI: `10.1029/93GL00831`.

Riese, M., F. Ploeger, A. Rap, B. Vogel, P. Konopka, M. Dameris and P. Forster (2012). 'Impact of uncertainties in atmospheric mixing on simulated UTLS composition and related radiative effects'. *J. Geophys. Res.*, 117, D16305. DOI: `10.1029/2012JD017751`.

Robock, A., C. M. Ammann, L. Oman, D. Shindell, S. Levis and G. Stenchikov (2009). 'Did the Toba volcanic eruption of 74 ka B.P. produce widespread glaciation?' *J. Geophys. Res.*, 114, D10107. DOI: `10.1029/2008JD011652`.

Robock, A. (2000). 'Volcanic eruptions and climate'. *Rev. Geophys.*, 38, pp. 191–219. DOI: `10.1029/1998RG000054`.

Russell, P. B., J. M. Livingston, E. G. Dutton, R. F. Pueschel, J. A. Reagan, T. E. DeFoor and D. J. Hofmann

(1993). 'Pinatubo and pre-Pinatubo optical-depth spectra: Mauna Loa measurements, comparisons, inferred particle size distributions, radiative effects, and relationship to lidar data'. *J. Geophys. Res.*, 98, pp. 22969–22985. DOI: `10.1029/93JD02308`.

Santee, M. L., A. Lambert, L. Froidevaux, G. L. Manney, M. J. Schwartz, L. F. Millán, N. J. Livesey, W. G. Read, F. Werner and R. A. Fuller (2023). 'Strong Evidence of Heterogeneous Processing on Stratospheric Sulfate Aerosol in the Extrapolar Southern Hemisphere Following the 2022 Hunga Tonga-Hunga Ha'apai Eruption'. *J. Geophys. Res.*, 128, e2023JD039169. DOI: `10.1029/2023jd039169`.

Santer, B. D., T. M. L. Wigley, C. Doutriaux, J. S. Boyle, J. E. Hansen, P. D. Jones and K. E. Taylor (2001). 'Accounting for the effects of volcanoes and ENSO in comparisons of modeled and observed temperature trends'. *J. Geophys. Res.*, 106, pp. 28033–28059. DOI: `10.1029/2000JD000189`.

Schoeberl, M. R., M. Toohey, Y. Wang and R. Ueyama (2025). 'Stratospheric Injection Lifetimes'. *J. Geophys. Res.*, 130, e2025JD043928. DOI: `10.1029/2025jd043928`.

Schoeberl, M. R., Y. Wang, G. Taha, D. J. Zawada, R. Ueyama and A. Dessler (2024). 'Evolution of the Climate Forcing During the Two Years After the Hunga Tonga-Hunga Ha'apai Eruption'. *J. Geophys. Res.*, 129, e2024JD041296. DOI: `10.1029/2024jd041296`.

Schoeberl, M. R., Y. Wang, R. Ueyama, G. Taha, E. Jensen and W. Yu (2022). 'Analysis and Impact of the Hunga Tonga-Hunga Ha'apai Stratospheric Water Vapor Plume'. *Geophys. Res. Lett.*, 49, e2022GL100248. DOI: `10.1029/2022gl100248`.

Schoeberl, M. R., Y. Wang, R. Ueyama, G. Taha and W. Yu (2023). 'The Cross Equatorial Transport of the Hunga Tonga-Hunga Ha'apai Eruption Plume'. *Geophys. Res. Lett.*, 50, e2022GL102443. DOI: `10.1029/2022gl102443`.

Sellitto, P., A. Podglajen, R. Belhadji, M. Boichu, E. Carboni, J. Cuesta, C. Duchamp, C. Kloss, R. Siddans, N. Bègue et al. (2022). 'The unexpected radiative impact of the Hunga Tonga eruption of 15th January 2022'. *Commun. Earth Environ.*, 3, 288. DOI: `10.1038/s43247-022-00618-z`.

Sellitto, P., R. Siddans, R. Belhadji, E. Carboni, B. Legras, A. Podglajen and et al. (2024). 'Observing the SO_2 and sulfate aerosol plumes from the 2022 Hunga eruption with the Infrared Atmospheric Sounding Interferometer (IASI)'. *Geophys. Res. Lett.*, 51, e2023GL105565. DOI: `10.1029/2023GL105565`.

Sherwood, S. C., S. Bony, O. Boucher, C. Bretherton, P. M. Forster, J. M. Gregory and B. Stevens (2015). 'Adjustments in the forcing-feedback framework for understanding climate change'. *Bull. Am. Meteorol. Soc.*, 96, pp. 217–228. DOI: `10.1175/bams-d-13-00167.1`.

Shindell, D. T., G. A. Schmidt, M. Mann and G. Faluvegi (2004). 'Dynamic winter climate response to large tropical volcanic eruptions since 1600'. *J. Geophys. Res.*, 109, D05104. DOI: `10.1029/2003JD004151`.

Shindell, D. T., G. A. Schmidt, R. L. Miller and M. Mann (2003). 'Volcanic and solar forcing of climate change during the preindustrial era'. *J. Climate*, 16, pp. 4094–4107. DOI: `10.1175/1520-0442(2003)016<4094:vasfoc>2.0.co;2`.

Sicard, M., A. Baron, M. Ranaivombola, D. Gantois, T. Millet, P. Sellitto, N. Bègue, H. Bencherif, G. Payen, N. Marquestaut et al. (2025). 'Radiative impact of the Hunga stratospheric volcanic plume: role of aerosols and water vapor over Réunion Island (21° S, 55° E)'. *Atmos. Chem. Phys.*, 25, pp. 367–381. DOI: `10.5194/acp-25-367-2025`.

Simpson, I. R., T. G. Shepherd and M. Sigmond (2011). 'Dynamics of the lower stratospheric circulation response to ENSO'. *J. Atmos. Sci.*, 68, pp. 2537–2556. DOI: `10.1175/jas-d-11-05.1`.

Smith, C. J., R. J. Kramer, G. Myhre, K. Alterskjær, W. Collins, A. Sima, O. Boucher, J.-L. Dufresne, P. Nabat and M. Michou (2020). 'Effective radiative forcing and adjustments in CMIP6 models'. *Atmos. Chem. Phys.*, 20, pp. 9591–9618. DOI: `10.5194/acp-20-9591-2020`.

Solomon, S., J. S. Daniel, R. R. Neely, J.-P. Vernier, E. G. Dutton and L. W. Thomason (2011). 'The Persistently Variable "Background" Stratospheric Aerosol Layer and Global Climate Change'. *Science*, 333, pp. 866–870. DOI: `10.1126/science.1206027`.

Solomon, S., K. H. Rosenlof, R. W. Portmann, J. S. Daniel, S. M. Davis, T. J. Sanford and G.-K. Plattner (2010). 'Contributions of Stratospheric Water Vapor to Decadal Changes in the Rate of Global Warming'. *Science*, 327, pp. 1219–1223. DOI: `10.1126/science.1182488`.

Stenchikov, G. (2016). 'The role of volcanic activity in climate and global change'. *Climate Change: Observed Impact on Planet Earth, 2nd Edition.* Ed. by T. Letcher. Elsevier, pp. 419–448.

Stenchikov, G., T. L. Delworth, V. Ramaswamy, R. J. Stouffer, A. Wittenberg and F. Zeng (2009). 'Volcanic signals in oceans'. *J. Geophys. Res.*, 114, D16104. DOI: `10.1029/2008jd011673`.

Stenchikov, G., K. Hamilton, A. Robock, V. Ramaswamy and M. D. Schwarzkopf (2004). 'Arctic Oscillation response to the 1991 Pinatubo eruption in the SKYHI GCM with a realistic quasi-biennial oscillation'. *J. Geophys. Res.*, 109, D03112. DOI: `10.1029/2003JD003699`.

Stenchikov, G., K. Hamilton, R. J. Stouffer, A. Robock, V. Ramaswamy, B. Santer and H.-F. Graf (2006). 'Arctic oscillation response to volcanic eruptions in the IPCC AR4 climate models'. *J. Geophys. Res.*, 111, D07107. DOI: `10.1029/2005JD006286`.

Stenchikov, G., A. Robock, V. Ramaswamy, M. D. Schwarzkopf, K. Hamilton and S. Ramachandran (2002). 'Arctic Oscillation response to the 1991 Mount Pinatubo eruption: effects of volcanic aerosols and ozone depletion'. *J. Geophys. Res.*, 107, 4803. DOI: `10.1029/2002JD002090`.

Stenchikov, G., A. Ukhov and S. Osipov (2025). 'Modeling the Radiative Forcing and Atmospheric Temperature Perturbations Caused by the 2022 Hunga Volcano Explosion'. *J. Geophys. Res.*, e2024JD041940. DOI: `10.1029/2024JD041940`.

Stenchikov, G., A. Ukhov, S. Osipov, R. Ahmadov, G. Grell, K. Cady-Pereira, E. Mlawer and M. Iacono (2021). 'How does a Pinatubo-size volcanic cloud reach the middle stratosphere?' *J. Geophys. Res.*, 126, e2020JD033829. DOI: `10.1029/2020jd033829`.

Stenchikov, G. L., I. Kirchner, A. Robock, H.-F. Graf, J. C. Antuña, R. G. Grainger, A. Lambert and L. Thomason (1998). 'Radiative forcing from the 1991 Mount Pinatubo volcanic eruption'. *J. Geophys. Res.*, 103, pp. 13837–13857. DOI: `10.1029/98jd00693`.

Swingedouw, D., J. Mignot, P. Ortega, M. Khodri, M. Menegoz, C. Cassou and V. Hanquiez (2017). 'Impact of explosive volcanic eruptions on the main climate variability modes'. *Global Planet. Change*, 150, pp. 24–45. DOI: `10.1016/j.gloplacha.2017.01.006`.

Taha, G., R. Loughman, P. R. Colarco, T. Zhu, L. W. Thomason and G. Jaross (2022). 'Tracking the 2022 Hunga Tonga-Hunga Ha'apai Aerosol Cloud in the Upper and Middle Stratosphere Using Space-Based Observations'. *Geophys. Res. Lett.*, 49, e2022GL100091. DOI: `10.1029/2022gl100091`.

Taha, G., R. Loughman, T. Zhu, L. Thomason, J. Kar, L. Rieger and A. Bourassa (2021). 'OMPS LP Version 2.0 multi-wavelength aerosol extinction coefficient retrieval algorithm'. *Atmos. Meas. Tech.*, 14, pp. 1015–1036. DOI: `10.5194/amt-14-1015-2021`.

Thomason, L. W., N. Ernest, L. Millán, L. Rieger, A. Bourassa, J.-P. Vernier, G. Manney, B. Luo, F. Arfeuille and T. Peter (2018). 'A global space-based stratospheric aerosol climatology: 1979–2016'. *Earth Syst. Sci. Data*, 10, pp. 469–492. DOI: `10.5194/essd-10-469-2018`.

Thompson, D. W. and J. M. Wallace (1998). 'The Arctic Oscillation signature in the wintertime geopotential height and temperature fields'. *Geophys. Res. Lett.*, 25, pp. 1297–1300. DOI: `10.1029/98GL00950`.

Thompson, D. W. and J. M. Wallace (2000). 'Annular modes in the extratropical circulation. Part I: Month-to-month variability'. *J. Climate*, 13, pp. 1000–1016. DOI: `10.1175/1520-0442(2000)013<1000:amitec>2.0.co;2`.

Tilmes, S., M. J. Mills, Y. Zhu, C. G. Bardeen, F. Vitt, P. Yu, D. Fillmore, X. Liu, B. Toon and T. Deshler (2023). 'Description and performance of a sectional aerosol microphysical model in the Community Earth System Model (CESM2)'. *Geosci. Model Dev.*, 16, pp. 6087–6125. DOI: `10.5194/gmd-16-6087-2023`.

Timmreck, C. (2012). 'Modeling the climatic effects of significant explosive volcanic eruptions'. *Wiley Interdiscip. Rev. Clim. Change*, 3, pp. 545–564. DOI: `10.1002/wcc.192`.

Timmreck, C., G. W. Mann, V. Aquila, R. Hommel, L. A. Lee, A. Schmidt, C. Brühl, S. Carn, M. Chin, S. S. Dhomse et al. (2018). 'The interactive stratospheric aerosol model intercomparison project (ISA-MIP): motivation and experimental design'. *Geosci. Model Dev.*, 11, pp. 2581–2608. DOI: `10.5194/gmd-11-2581-2018`.

Toohey, M., Y. Jia, S. Khanal and S. Tegtmeier (2025). 'Stratospheric residence time and the lifetime of volcanic stratospheric aerosols'. *Atmos. Chem. Phys.*, 25, pp. 3821–3839. DOI: `10.5194/acp-25-3821-2025`.

Trepte, C. R. and M. H. Hitchman (1992). 'Tropical stratospheric circulation deduced from satellite aerosol data'. *Nature*, 355, pp. 626–628. DOI: `10.1038/355626a0`.

Turco, R. P., R. C. Witten and O. B. Toon (1982). 'Stratospheric Aerosols: Observation and Theory'. *Rev. Geophys. Space Phys.*, 20, pp. 233–279. DOI: `10.1029/RG020i002p00233`.

Vömel, H., S. Evan and M. Tully (2022). 'Water vapor injection into the Stratosphere by Hunga Tonga-Hunga Ha'apai'. *Science*, 377, pp. 1444–1447. DOI: `10.1126/science.abq2299`.

Vömel, H., S. J. Oltmans, D. J. Hofmann, T. Deshler and J. M. Rosen (1995). 'The evolution of the dehydration in the Antarctic stratospheric vortex'. *J. Geophys. Res.*, 100, pp. 13919–13926. DOI: `10.1029/95JD01000`.

Wallis, S., M. DeLand and C. von Savigny (2025). 'Did the 2022 Hunga eruption impact the noctilucent cloud season in 2023/24 and 2024?' *Atmos. Chem. Phys.*, 25, pp. 3635–3645. DOI: `10.5194/acp-25-3635-2025`.

Walsh, A., J. A. Screen, A. A. Scaife and D. M. Smith (2022). 'Non-Linear response of the extratropics to tropical climate variability'. *Geophys. Res. Lett.*, 49, e2022GL100416. DOI: `10.1029/2022GL100416`.

Wang, J., S. Park, J. Zeng, C. Ge, K. Yang, S. Carn, N. Krotkov and A. H. Omar (2013). 'Modeling of 2008 Kasatochi volcanic sulfate direct radiative forcing: assimilation of OMI SO 2 plume height data and comparison with MODIS and CALIOP observations'. *Atmos. Chem. Phys.*, 13, pp. 1895–1912. DOI: `10.5194/acp-13-1895-2013`.

Wang, X., W. Randel, Y. Zhu, S. Tilmes, J. Starr, W. Yu, R. Garcia, O. B. Toon, M. Park, D. Kinnison et al. (2023). 'Stratospheric Climate Anomalies and Ozone Loss Caused by the Hunga Tonga-Hunga Ha'apai Volcanic Eruption'. *J. Geophys. Res.*, 128, e2023JD039480. DOI: `10.1029/2023jd039480`.

Wang, Y. and Y. Huang (2024). 'Compensating atmospheric adjustments reduce the volcanic forcing from Hunga stratospheric water vapor enhancement'. *Sci. Adv.*, 10, eadl2842. DOI: `10.1126/sciadv.adl2842`.

Waugh, D. W. and L. M. Polvani (2010). 'Stratospheric polar vortices'. *The stratosphere: Dynamics, transport, and chemistry.* Ed. by L. M. Polvani, A. H. Sobel and D. W. Waugh. Vol. 190. Geophysical Monograph Series. American Geophysical Union, pp. 43–57. DOI: `10.1029/GM190`.

Wetherald, R. T. and S. Manabe (1988). 'Cloud feedback processes in a general circulation model'. *J. Atmos. Sci.*, 45, pp. 1397–1416. DOI: `10.1175/1520-0469(1988)045<1397:CFPIAG>2.0.CO;2`.

Wilmouth, D. M., F. F. Østerstrøm, J. B. Smith, J. G. Anderson and R. J. Salawitch (2023). 'Impact of the Hunga Tonga volcanic eruption on stratospheric composition'. *Proc. Natl. Acad. Sci.*, 120, e2301994120. DOI: `10.1073/pnas.2301994120`.

Witze, A. (2022). 'Why the Tongan eruption will go down in the history of volcanology'. *Nature*, 602, pp. 376–378. DOI: `10.1038/d41586-022-00394-y`.

Yook, S., S. Solomon and X. Wang (2025). 'The impact of 2022 Hunga Tonga-Hunga Ha'apai (Hunga) eruption on stratospheric circulation and climate'. *J. Geophys. Res.*, 130, e2024JD042943. DOI: `10.1029/2024JD042943`.

Yu, P., R. W. Portmann, Y. Peng, C.-C. Liu, Y. Zhu, E. Asher, Z. Bai, Y. Lu, J. Bian, M. Mills et al. (2023a). 'Radiative Forcing From the 2014–2022 Volcanic and Wildfire Injections'. *Geophys. Res. Lett.*, 50, e2023GL103791. DOI: `10.1029/2023GL103791`.

Yu, Q. and Y. Huang (2023). 'A Dissection of the Inter-Model Spread of the Aerosol Direct Radiative Effect in CMIP6 Models'. *Geophys. Res. Lett.*, 50, e2023GL105112. DOI: `10.1029/2023GL105112`.

Yu, Q. and Y. Huang (2024). 'Quantifying the Direct Radiative Effect of Stratospheric Aerosols Using Radiative Kernels'. *ESS Open Archive*, DOI: `10.22541/essoar.172374105.56686934/v1`.

Yu, W., R. Garcia, J. Yue, A. Smith, X. Wang, W. Randel, Z. Qiao, Y. Zhu, V. L. Harvey, S. Tilmes et al. (2023b). 'Mesospheric temperature and circulation response to the Hunga Tonga-Hunga-Ha'apai volcanic eruption'. *J. Geophys. Res.*, 128, e2023JD039636. DOI: `10.1029/2023JD039636`.

Zhang, H., F. Wang, J. Li, Y. Duan, C. Zhu and J. He (2022). 'Potential Impact of Tonga Volcano Eruption on Global Mean Surface Air Temperature'. *J. Meteorol. Res.*, 36, pp. 1–5. DOI: `10.1007/s13351-022-2013-6`.

Zhang, J., D. Kinnison, Y. Zhu, X. Wang, S. Tilmes, K. Dube and W. Randel (2024). 'Chemistry Contribution to Stratospheric Ozone Depletion After the Unprecedented Water-Rich Hunga Tonga Eruption'. *Geophys. Res. Lett.*, 51, e2023GL105762. DOI: `10.1029/2023gl105762`.

Zhou, X., S. S. Dhomse, W. Feng, G. Mann, S. Heddell, H. Pumphrey, B. J. Kerridge, B. Latter, R. Siddans, L. Ventress et al. (2024). 'Antarctic Vortex Dehydration in 2023 as a Substantial Removal Pathway for Hunga Tonga-Hunga Ha'apai Water Vapor'. *Geophys. Res. Lett.*, 51, e2023GL107630. DOI: `10.1029/2023gl107630`.

Zhu, Y., C. G. Bardeen, S. Tilmes, M. J. Mills, X. Wang, V. L. Harvey, G. Taha, D. Kinnison, R. W. Portmann, P. Yu et al. (2022). 'Perturbations in stratospheric aerosol evolution due to the water-rich plume of the 2022 Hunga-Tonga eruption'. *Commun. Earth Environ.*, 3, 248. DOI: `10.1038/s43247-022-00580-w`.

Zhuo, Z., X. Wang, Y. Zhu, W. Yu, E. M. Bednarz, E. Fleming, P. R. Colarco, S. Watanabe, D. Plummer, G. Stenchikov et al. (2025). 'Comparing multi-model ensemble simulations with observations and decadal projections of upper atmospheric variations following the Hunga eruption'. *Atmos. Chem. Phys.*, 25, pp. 13161–13176. DOI: `10.5194/acp-25-13161-2025`.